Computers and Mathematics with Applications 72 (2016) 288–310

Contents lists available at ScienceDirect

Computers and Mathematics with Applications

journal homepage: www.elsevier.com/locate/camwa

Designing correct fluid hydrodynamics on a rectangular grid using MRT lattice Boltzmann approach

Yuan Zong [a,b], Cheng Peng [b], Zhaoli Guo [c], Lian-Ping Wang [b,c,*]

[a] State Key Laboratory of Chemical Engineering, East China University of Science and Technology, Shanghai, 200237, PR China
[b] Department of Mechanical Engineering, 126 Spencer Laboratory, University of Delaware, Newark, DE 19716-3140, USA
[c] National Laboratory of Coal Combustion, Huazhong University of Science and Technology, Wuhan, 430074, PR China

ARTICLE INFO

Article history:
Available online 13 June 2015

Keywords:
Rectangular grid
Multiple-relaxation time
Lattice Boltzmann method
Navier–Stokes equations

ABSTRACT

While the lattice Boltzmann method (LBM) has become a powerful numerical approach for solving complex flows, the standard lattice Boltzmann method typically uses a square lattice grid in two spatial dimensions and cubic lattice grid in three dimensions. For inhomogeneous and anisotropic flows, it is desirable to have a LBM model that utilizes a rectangular grid. There were two previous attempts to extend the multiple-relaxation-time (MRT) LBM to a rectangular lattice grid in 2D, however, the resulting hydrodynamic momentum equation was not fully consistent with the Navier–Stokes equation, due to anisotropy of the transport coefficients. In the present work, a new MRT model with an additional degree of freedom is developed in order to match precisely the Navier–Stokes equation when a rectangular lattice grid is used. We first revisit the previous attempts to understand the origin and nature of anisotropic transport coefficients by conducting an inverse design analysis within the Chapman–Enskog procedure. Then an additional adjustable parameter that governs the relative orientation in the energy–normal stress subspace is introduced. It is shown that this adjustable parameter can be used to fully eliminate the anisotropy of transport coefficients, thus the exact Navier–Stokes equation can be derived on a rectangular grid. Our theoretical findings are confirmed by numerical solutions using three two-dimension benchmark problems, *i.e.* the channel flow, the cavity flow, and the decaying Taylor–Green vortex flow. The numerical results demonstrate that the proposed model shows remarkably good performance with appropriate choice of model parameters.

© 2015 Elsevier Ltd. All rights reserved.

1. Introduction

As an alternative numerical method based on kinetic theory, the lattice Boltzmann method (LBM) has attracted a great deal of attention since its inception about 25 years ago [1,2]. The basic idea is to design a fully discrete version of the Boltzmann equation, with a minimum set of discrete microscopic velocities, that can yield the exact Navier–Stokes equation through the Chapman–Enskog analysis. From a computational viewpoint, the advantages of LBM include its algorithm simplicity, intrinsic data locality (thus straightforward to perform parallel computation), and capability to conveniently incorporate complex fluid–solid and fluid–fluid boundary conditions. Hence, LBM has been widely employed in simulations

* Corresponding author at: Department of Mechanical Engineering, 126 Spencer Laboratory, University of Delaware, Newark, DE 19716-3140, USA.
E-mail addresses: zongyuan@ecust.edu.cn (Y. Zong), cpengxpp@udel.edu (C. Peng), zlguo@hust.edu.cn (Z. Guo), lwang@udel.edu (L.-P. Wang).

http://dx.doi.org/10.1016/j.camwa.2015.05.021
0898-1221/© 2015 Elsevier Ltd. All rights reserved.

of complex fluid systems, such as multiphase flows [3,4], complex viscous flows with deformable boundary and complex geometry such as porous media [5–7], and micro-scale flows [8,9].

Despite the success of LBM, the standard LBM is restricted to a square grid or hexagonal grid in two spatial dimensions (2D) and a cubic grid in three spatial dimensions (3D). This restriction is aligned with the set of microscopic velocities used and is desirable for model isotropy. However, this could result in a low computational efficiency when the flow field is highly nonuniform, inhomogeneous, and anisotropic, such as a boundary layer flow where the velocity gradients in one spatial dimension is much stronger than the other directions. To alleviate this problem within LBM, different approaches have been developed to allow the use of a nonuniform grid. One approach is to employ an interpolation method to decouple the grid associated with lattice Boltzmann microscopic velocities, from the numerical mesh. Pioneering work in this direction includes the studies of Filippova and Hänel [10,11] who reconstructed distribution functions at arbitrary locations using spatial and temporal interpolations. Another approach is to introduce local grid refinement or use different mesh densities for different regions of the flow (*i.e.*, multi-block methods) [12]. Methods to communicate distribution functions, defined on coarse and fine grids, at the block interfaces have been developed. Other methods to use a non-uniform grid typically utilize a local interpolation scheme [13,14]. While these approaches have been actively extended and applied in many applications, their accuracy is limited by the interpolation scheme which may also introduce additional artificial dissipation. Therefore, it is desirable to construct a lattice Boltzmann method with a more flexible grid that is free of interpolation.

Inspired by the work of Koelman [15], Bouzidi et al. [16] made the first attempt to construct a multiple-relaxation-time (MRT) LBM on a two-dimensional rectangular grid. The model showed good performance with appropriate choice of model parameters, but the resulting hydrodynamic momentum equation is not fully consistent with the Navier–Stokes equations. Another attempt was made by Zhou [17] who redefined the moments so that the transformation matrix for a rectangular grid was identical to that for a standard MRT on a square grid. However, the modifications suggested in Zhou [17] led to anisotropic fluid viscosity. Hegele et al. [18] indicated some extra degrees of freedom should be employed to satisfy the isotropy conditions for rectangular lattice Boltzmann scheme. There are three possible approaches: decoupling the discretizations of the velocity space from spatial and temporal discretization, modification of a collision operator with additional parameter, and adoption of more discrete microscopic velocities. They introduced two extra microscopic velocities to extend the D2Q9 model with BGK collision operator and were able to restore, on a rectangular grid, the isotropy condition required for the Navier–Stokes equation. They also suggested that four new velocities are needed in order to correctly extend the D3Q19 model onto a noncubic 3D grid.

In the present work, we explore the possibility to restore the isotropy condition on a 2D rectangular grid without introducing any additional microscopic velocity. We take advantage of some of the flexibility within the MRT LBM scheme [19,20]. For this purpose, we will introduce an additional parameter in the energy–normal stress moment subspace. Before presenting our novel MRT LBM scheme on a rectangular grid, previous MRT schemes on a rectangular grid are firstly reviewed in Section 2. An inverse design analysis will be used to derive the equilibrium moments and the anisotropy of the transport coefficients for a rectangular grid is revealed. In Section 3, our new scheme with an additional free parameter is constructed in order to restore the isotropy for a rectangular grid, namely, the usual Navier–Stokes hydrodynamic equations are derived using a rectangular grid. Also, the coupling relationships between relaxations times and determination of computational parameters are re-interpreted, which enables the flexibility to choose computational parameters according to different flow problems. In Section 4, numerical validation of our new scheme is provided using a 2D channel flow, a 2D lid-driven cavity flow and 2D Taylor–Green vortex flow. Concluding remarks are provided in Section 5.

2. An analysis of previous MRT LBM schemes on a rectangular grid

2.1. The model of Bouzidi et al. [16]

We begin with the MRT LBM scheme [19] in 2D, which has been shown to provide more flexibility in relaxing different moments and to significantly improve computational stability and accuracy, while simplicity and computational efficiency of LBM are retained. However, we consider a rectangular grid as shown in Fig. 1, where the non-zero lattice velocity in the x direction is one, and in the y direction is a ($a < 1$). Following the spirit of the D2Q9 model but with the different velocities in x and y directions, the discrete velocities are defined as

$$\mathbf{e}_i = \begin{cases} (0,0) & i = 0 \\ (\pm 1, 0), (0, \pm a) & i = 1-4 \\ (\pm 1, \pm a) & i = 5-8. \end{cases} \tag{1}$$

The distribution functions in MRT LBM evolve as

$$f_i(\mathbf{x} + \mathbf{e}_i \delta t) - f_i(\mathbf{x}, t) = \Omega_i \tag{2}$$

where f_i is the distribution function associated with the molecular velocity $\mathbf{e}_i$ at position $\mathbf{x}$ and time t, Ω_i is the collision operator.

In MRT LBM, the streaming process takes place in the physical space while the collision process is performed in the moment space. The nine distribution functions define nine degrees of freedom, which implies that nine independent moments

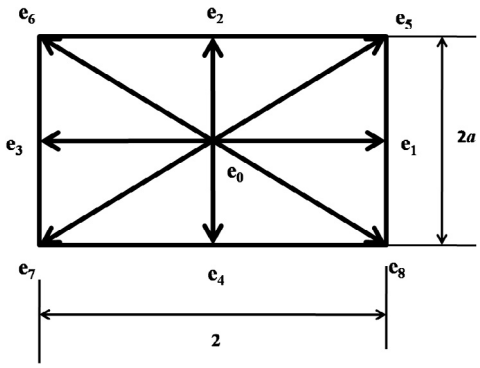

Fig. 1. Discrete velocities of the D2Q9 MRT model on a rectangular grid. The aspect ratio of the grid is $\delta_y/\delta_x = a$.

can be constructed. We first adopt the moments introduced in Bouzidi et al. [16] through a transformation matrix M

$$\mathbf{m} = Mf \tag{3}$$

where $f = (f_0, f_1, f_2, f_3, f_4, f_5, f_6, f_7, f_8)^T$. The transformation matrix M specifies the nature of the moments and is given as [16]

$$M = \begin{pmatrix} 1 & 1 & 1 & 1 & 1 & 1 & 1 & 1 & 1 \\ -2r_1 & r_2 & r_3 & r_2 & r_3 & r_1 & r_1 & r_1 & r_1 \\ 4 & -2 & -2 & -2 & -2 & 1 & 1 & 1 & 1 \\ 0 & 1 & 0 & -1 & 0 & 1 & -1 & -1 & 1 \\ 0 & -2 & 0 & 2 & 0 & 1 & -1 & -1 & 1 \\ 0 & 0 & a & 0 & -a & a & a & -a & -a \\ 0 & 0 & -2a & 0 & 2a & a & a & -a & -a \\ -2r_4 & r_5 & r_6 & r_5 & r_6 & r_4 & r_4 & r_4 & r_4 \\ 0 & 0 & 0 & 0 & 0 & 1 & -1 & 1 & -1 \end{pmatrix} \tag{4}$$

where $r_1 = 1 + a^2$, $r_2 = 1 - 2a^2$, $r_3 = -2 + a^2$, $r_4 = -1 + a^2$, $r_5 = 2 + a^2$, $r_6 = -1 - 2a^2$. The row vectors are orthogonal and they define the following nine moments

$$\mathbf{m} = \left(\rho, e, \varepsilon, j_x, q_x, j_y, q_y, p_{xx}, p_{xy}\right)^T, \tag{5}$$

where ρ is the density, e is the kinetic energy, ε is the kinetic energy squared, j_x and j_y are the momentum density in the x and y directions, respectively. q_x and q_y are the x and y components of the energy flux, p_{xx} and p_{xy} are related to the diagonal and off-diagonal components of the viscous stress tensor.

The MRT collision operator Ω_i is expressed as

$$\mathbf{\Omega} = -M^{-1}SM\left[f(x,t) - f^{eq}(x,t)\right] \tag{6}$$

where S is a non-negative diagonal relaxation matrix,

$$S = \text{diag}\left(s_\rho, s_e, s_\varepsilon, s_j, s_q, s_j, s_q, s_n, s_c\right) \tag{7}$$

where s_n and s_c are the relaxation times for p_{xx} and p_{xy}, respectively. When all the relaxation times are set to be equal, the usual BGK model is recovered.

We shall now perform the Chapman–Enskog multiscaling analysis in order to derive the macroscopic hydrodynamic equations. To this end, we first expand the distribution function f_i, the derivatives in time and space as [1,21]

$$\mathbf{m} = \mathbf{m}^{(0)} + \epsilon\mathbf{m}^{(1)} + \epsilon^2\mathbf{m}^{(2)} + \cdots, \tag{8a}$$

$$\frac{\partial}{\partial t} = \epsilon\partial_{t_1} + \epsilon^2\partial_{t_2}, \tag{8b}$$

$$\frac{\partial}{\partial x_\alpha} = \epsilon\partial_{1\alpha}, \tag{8c}$$

where ϵ is a small parameter which is proportional to the ratio of the lattice spacing to a characteristic macroscopic length.

Performing Taylor expansion for Eq. (2) and substituting the above expansions, the following equations at zeroth-, first- and second-order in ϵ can be obtained

$$\mathcal{O}(\epsilon^0) : \mathbf{m}^{(0)} = \mathbf{m}^{(eq)}, \tag{9a}$$

$$\mathcal{O}(\epsilon^1) : \left(I\partial_{t_1} + \hat{C}_\alpha \partial_{1\alpha}\right)\mathbf{m}^{(0)} = -\frac{S}{\Delta t}\mathbf{m}^{(1)}, \tag{9b}$$

$$\mathcal{O}(\epsilon^2) : \partial_{t_2}\mathbf{m}^{(0)} + \left(I\partial_{t_1} + \hat{C}_\alpha \partial_{1\alpha}\right)\left(I - \frac{S}{2}\right)\mathbf{m}^{(1)} = -\frac{S}{\Delta t}\mathbf{m}^{(2)}, \tag{9c}$$

where $\hat{C}_\alpha = M\mathrm{diag}(e_{0\alpha}, e_{1\alpha}, \ldots, e_{8\alpha})M^{-1}$. Eq. (9c) has already been simplified by making use of Eq. (9b).

The first, fourth and sixth components of Eq. (9b) are

$$\partial_{t_1}\rho + \partial_{1x}j_x^{(eq)} + \partial_{1y}j_y^{(eq)} = 0 \tag{10a}$$

$$\partial_{t_1}j_x^{(eq)} + \partial_{1x}\left[\frac{2}{3}\rho + \frac{e^{(eq)}}{3(a^4+1)} + \frac{a^2}{3(a^4+1)}p_{xx}^{(eq)}\right] + \partial_{1y}\left(ap_{xy}^{(eq)}\right) = 0 \tag{10b}$$

$$\partial_{t_1}j_y^{(eq)} + \partial_{1x}\left(ap_{xy}^{(eq)}\right) + \partial_{1y}\left[\frac{2a^2}{3}\rho + \frac{a^4e^{(eq)}}{3(a^4+1)} - \frac{a^2}{3(a^4+1)}p_{xx}^{(eq)}\right] = 0. \tag{10c}$$

The design target at $\mathcal{O}(\epsilon)$ is the Euler equations

$$\partial_{t_1}\rho + \partial_{1x}\left(\rho u_x\right) + \partial_{1y}\left(\rho u_y\right) = 0, \tag{11a}$$

$$\partial_{t_1}\left(\rho u_x\right) + \partial_{1x}\left(\rho c_s^2 + \rho u_x^2\right) + \partial_{1y}\left(\rho u_x u_y\right) = 0, \tag{11b}$$

$$\partial_{t_1}\left(\rho u_y\right) + \partial_{1x}\left(\rho u_x u_y\right) + \partial_{1y}\left(\rho c_s^2 + \rho u_y^2\right) = 0, \tag{11c}$$

where the pressure has been written as $p = \rho c_s^2$. Comparing Eq. (10) to Eq. (11), we obtain

$$j_x^{(eq)} = \rho u_x, \qquad j_y^{(eq)} = \rho u_y, \tag{12a}$$

$$\frac{2}{3}\rho + \frac{e^{(eq)}}{3(a^4+1)} + \frac{a^2}{3(a^4+1)}p_{xx}^{(eq)} = \rho(c_s^2 + u_x^2), \tag{12b}$$

$$\frac{2a^2}{3}\rho + \frac{a^4e^{(eq)}}{3(a^4+1)} - \frac{a^2}{3(a^4+1)}p_{xx}^{(eq)} = \rho(c_s^2 + u_y^2), \tag{12c}$$

$$ap_{xy}^{(eq)} = \rho u_x u_y. \tag{12d}$$

These can be solved to yield three equilibrium moments in addition to $j_x^{(eq)}$ and $j_y^{(eq)}$ as

$$e^{(eq)} = \rho\left[2\left(3c_s^2 - r_1\right) + 3u^2\right], \tag{13a}$$

$$p_{xx}^{(eq)} = \rho\left[\frac{r_4}{a^2}\left(3r_1c_s^2 - 2a^2\right) + 3\left(a^2u_x^2 - \frac{u_y^2}{a^2}\right)\right], \tag{13b}$$

$$p_{xy}^{(eq)} = \rho\frac{u_x u_y}{a}. \tag{13c}$$

At this point, the remaining three equilibrium moments, *i.e*, $\varepsilon^{(eq)}$, $q_x^{(eq)}$ and $q_y^{(eq)}$, are to be determined. As we will realize soon that $\varepsilon^{(eq)}$ does not affect the Navier–Stokes equations, it can be defined somewhat arbitrarily. $q_x^{(eq)}$ and $q_y^{(eq)}$ will be determined by the hydrodynamic equation at $\mathcal{O}(\epsilon^2)$.

At $\mathcal{O}\left(\epsilon^2\right)$, the first, fourth, and sixth components of Eq. (9c) yield

$$\partial_{t_2}\rho = 0, \tag{14a}$$

$$\partial_{t_2}(\rho u_x) = -\frac{a^2\left(1 - 0.5s_n\right)}{3\left(a^4+1\right)}\partial_{1x}p_{xx}^{(1)} - a\left(1 - 0.5s_c\right)\partial_{1y}p_{xy}^{(1)} - \frac{1 - 0.5s_e}{3\left(a^4+1\right)}\partial_{1x}e^{(1)}, \tag{14b}$$

$$\partial_{t_2}(\rho u_y) = \frac{a^2\left(1 - 0.5s_n\right)}{3\left(a^4+1\right)}\partial_{1y}p_{xx}^{(1)} - a\left(1 - 0.5s_c\right)\partial_{1x}p_{xy}^{(1)} - \frac{a^4\left(1 - 0.5s_e\right)}{3\left(a^4+1\right)}\partial_{1y}e^{(1)}. \tag{14c}$$

The design target at $\mathcal{O}(\epsilon^2)$ is to potentially match the Navier–Stokes equation which may be stated in a more general form as:

$$\partial_{t_2}(\rho u_x) = \partial_{1x}\left[\rho\zeta_x\left(\partial_{1x}u_x + \partial_{1y}u_y\right) + \rho\nu_x\left(\partial_{1x}u_x - \partial_{1y}u_y\right)\right] + \partial_{1y}\left[\rho\nu\left(\partial_{1y}u_x + \partial_{1x}u_y\right)\right], \tag{15a}$$

$$\partial_{t_2}(\rho u_y) = \partial_{1x}\left[\rho\nu\left(\partial_{1y}u_x + \partial_{1x}u_y\right)\right] + \partial_{1y}\left[\rho\zeta_y\left(\partial_{1x}u_x + \partial_{1y}u_y\right) + \rho\nu_y\left(\partial_{1y}u_y - \partial_{1x}u_x\right)\right], \tag{15b}$$

where ζ_x and ζ_y are bulk viscosities in x and y directions, respectively; ν_x and ν_y are two viscosities associated with normal viscous stress components, and ν is the shear viscosity.

At this point, we need the explicit expressions for $e^{(1)}$, $p_{xx}^{(1)}$, and $p_{xy}^{(1)}$ which can be obtained from Eq. (9b). They are

$$-s_e' e^{(1)} = \partial_{t_1}\left[2\rho\left(3c_s^2 - r_1\right) + 3\rho u^2\right] + \partial_{1x}\left(j_x^{(eq)} + a^2 q_x^{(eq)}\right) + \partial_{1y}\left(a^2 j_y^{(eq)} + q_y^{(eq)}\right), \tag{16a}$$

$$-s_n' p_{xx}^{(1)} = \partial_{t_1}\left[\frac{\rho r_4}{a^2}\left(3r_1c_s^2 - 2a^2\right) + 3\rho\left(a^2u_x^2 - \frac{u_y^2}{a^2}\right)\right] + \partial_{1x}\left(a^2 j_x^{(eq)} - q_x^{(eq)}\right) + \partial_{1y}\left(-j_y^{(eq)} + a^2 q_y^{(eq)}\right), \tag{16b}$$

$$-s_c' p_{xy}^{(1)} = \partial_{t_1}\left(\frac{\rho u_x u_y}{a}\right) + \partial_{1x}\left(\frac{2}{3a}j_y^{(eq)} + \frac{1}{3a}q_y^{(eq)}\right) + \partial_{1y}\left(\frac{2a}{3}j_x^{(eq)} + \frac{a}{3}q_x^{(eq)}\right), \tag{16c}$$

where $s_i' = s_i/\delta t$. It is noted that the $\partial_{t_1}[\ldots]$ terms in the above equations involve $\partial_{t_1}(\rho u_\alpha u_\beta)$, which can be converted to spatial derivatives using the Euler equations as

$$\partial_{t_1}\left(\rho u_\alpha u_\beta\right) = -u_\alpha\partial_{1\beta}p - u_\beta\partial_{1\alpha}p + \mathcal{O}(u^3). \tag{17}$$

Since, at low Mach number, $p = \mathcal{O}(Ma^2)$, we conclude that $\partial_{t_1}(\rho u_\alpha u_\beta) = \mathcal{O}(u^3)$ and thus can be neglected.

Comparing Eq. (15) with Eq. (16), it is obvious that only $p_{xy}^{(1)}$ contributes to the cross shear stress term. To match the form of $\left(\partial_{1y}u_x + \partial_{1x}u_y\right)$ required by the Navier–Stokes equations, we must demand that $q_x^{(eq)} = \gamma_1 j_x^{(eq)}/2 = \gamma_1\rho u_x/2$ and $q_y^{(eq)} = \gamma_2 j_y^{(eq)}/2 = \gamma_2\rho u_y/2$, where γ_1 and γ_2 are constants to be determined. Furthermore, the net coefficients for the $\partial_{1y}u_x$ term and $\partial_{1x}u_y$ term must be made identical, namely,

$$\frac{2}{3a} + \frac{1}{6a}\gamma_2 = \frac{2a}{3} + \frac{a}{6}\gamma_1. \tag{18}$$

This implies that γ_1 can be determined in terms of γ_2 as

$$\gamma_1 = \frac{\gamma_2 + 4(1-a^2)}{a^2}. \tag{19}$$

This is identical to Eq. (3.6) in Bouzidi et al. [16] since our γ_1 and γ_2 are denoted by c_1 and c_2 in their paper. In the following, we denote γ_2 by γ. At this point, we have determined all necessary equilibrium moments which could affect the hydrodynamic equations.

Substituting Eq. (16) into Eq. (14) with the forms of the equilibrium moments already determined, we can derive the explicit expression of each transport coefficient that appears in Eq. (15). The results are

$$\nu_x = \frac{\Delta t}{2(a^4+1)}(1-a^2)\left(\frac{1}{s_e} - 0.5\right) + \frac{a^2\Delta t}{6(a^4+1)}\left(a^2 - \frac{\gamma}{2a^2} - \frac{2}{a^2} - \frac{a^2\gamma}{2} + 3\right)\left(\frac{1}{s_n} - 0.5\right), \tag{20a}$$

$$\begin{aligned}\zeta_x \;=\; & \frac{\Delta t}{6(a^4+1)}\left(7 + \gamma + 3a^2 - 12c_s^2\right)\left(\frac{1}{s_e} - 0.5\right) \\ & + \frac{a^2\Delta t}{6\left(a^4+1\right)}\left(5a^2 - \frac{2}{a^2} - \frac{\gamma}{2a^2} - 6a^2c_s^2 + 6\frac{c_s^2}{a^2} + \frac{a^2\gamma}{2} - 3\right)\left(\frac{1}{s_n} - 0.5\right),\end{aligned} \tag{20b}$$

$$\nu_y = \frac{a^4\Delta t}{2(a^4+1)}(a^2-1)\left(\frac{1}{s_e} - 0.5\right) + \frac{a^2\Delta t}{6(a^4+1)}\left(a^2 - \frac{\gamma}{2a^2} - \frac{2}{a^2} - \frac{a^2\gamma}{2} + 3\right)\left(\frac{1}{s_n} - 0.5\right), \tag{20c}$$

$$\begin{aligned}\zeta_y \;=\; & \frac{a^4\Delta t}{6(a^4+1)}\left(7 + \gamma + 3a^2 - 12c_s^2\right)\left(\frac{1}{s_e} - 0.5\right) \\ & - \frac{a^2\Delta t}{6(a^4+1)}\left(5a^2 - \frac{2}{a^2} - \frac{\gamma}{2a^2} - 6a^2c_s^2 + 6\frac{c_s^2}{a^2} + \frac{a^2\gamma}{2} - 3\right)\left(\frac{1}{s_n} - 0.5\right),\end{aligned} \tag{20d}$$

$$\nu = \frac{\gamma+4}{6}\left(\frac{1}{s_c} - 0.5\right)\Delta t. \tag{20e}$$

It can be seen from Eq. (20), the hydrodynamic transport coefficients on a rectangular grid depend on parameters c_s, γ, s_e, s_n, s_c and the grid parameter a. The question here is whether we can achieve the isotropy conditions required

by the Navier–Stokes equations: $\nu = \nu_x = \nu_y$ and $\zeta_x = \zeta_y$ (together they represent three conditions). Since the relaxation parameters are directly related to the various transport coefficients, Bouzidi et al. [16] attempted to approach the isotropy conditions by relating s_e and s_n to s_c, using a linearized dispersion analysis. Here we shall derive the same relationships from a very different perspective.

First, we define an average bulk viscosity as

$$\zeta \equiv \frac{\zeta_x + \zeta_y}{2} = \frac{\left(7 + \gamma + 3a^2 - 12c_s^2\right)}{12}\left(\frac{1}{s_e} - 0.5\right)\Delta t \tag{21}$$

which is identical to the expression of bulk viscosity in Bouzidi et al. [16]. In order to construct the coupling relationships between the relaxation parameters, we impose the following two conditions

$$\nu = \frac{\nu_x + \nu_y}{2}, \tag{22a}$$

$$\frac{\zeta_x - \zeta_y}{2} + \frac{\nu_x - \nu_y}{2} = 0. \tag{22b}$$

The first condition states that the average normal shear viscosity should be the same as the cross shear viscosity, which represents one step toward the isotropy conditions. The second condition amounts to $\nu_x + \zeta_x = \nu_y + \zeta_y$, namely, the net normal viscosities in the x and y directions are the same. Herein, we can build two coupling relationships between s_e, s_n and s_c. The true isotropy involves three conditions, here we impose two conditions first.

Substituting the expressions of the transport coefficients in Eq. (20) into Eq. (22), we can express s_e and s_n in terms of s_c as follows

$$\frac{1}{s_e} - \frac{1}{2} = \frac{2\left(4+\gamma\right)\left[\left(12c_s^2 - \gamma\right)\left(1+a^2\right) - 2\left(5a^2+2\right)\right]}{\left(1+a^2\right)\left(1+\gamma-3a^2\right)\left(\gamma+10-12c_s^2\right) + 6\left[a^4\left(\gamma-2\right) - 3\left(a^2-1\right)\right]}\left(\frac{1}{s_c} - \frac{1}{2}\right), \tag{23}$$

$$\frac{1}{s_n} - \frac{1}{2} = \frac{2\left(4+\gamma\right)\left[\left(12c_s^2 - \gamma\right)\left(1+a^2\right) - 2\left(3a^4+5a^2+5\right)\right]}{\left(1+a^2\right)\left(1+\gamma-3a^2\right)\left(\gamma+10-12c_s^2\right) + 6\left[a^4\left(\gamma-2\right) - 3\left(a^2-1\right)\right]}\left(\frac{1}{s_c} - \frac{1}{2}\right), \tag{24}$$

which are precisely the two relationships proposed in Bouzidi et al. [16] based on the linearized dispersion analysis.

An important detail should be noted. In the above derivation the limit of $a \to 1$ is a singular limit. In this limit, the first condition, Eq. (22a), will yield

$$\frac{\left(2-\gamma\right)\Delta t}{12}\left(\frac{1}{s_n} - 0.5\right) = \frac{\left(4+\gamma\right)\Delta t}{6}\left(\frac{1}{s_c} - 0.5\right). \tag{25}$$

The second condition, Eq. (22b), leads to a condition

$$\begin{aligned}\left(1-a^2\right)\Bigg\{&\left[\left(12c_s^2 - \gamma - 4\right)\left(1-a^4\right) - 6a^2\right]\left(\frac{1}{s_n} - 0.5\right)\\ &+ \left[\left(7+\gamma+3a^2-12c_s^2\right)\left(1+a^2\right) + 3\left(1+a^2\right)\right]\left(\frac{1}{s_e} - 0.5\right)\Bigg\} = 0\end{aligned} \tag{26}$$

which is automatically satisfied when $a = 1$. Further deriving the relationships, Eqs. (23) and (24), however, we did not use the condition of $a = 1$ but instead set

$$\left[\left(12c_s^2 - \gamma - 4\right)\left(1-a^4\right) - 6a^2\right]\left(\frac{1}{s_n} - 0.5\right) + \left[\left(7+\gamma+3a^2-12c_s^2\right)\left(1+a^2\right) + 3\left(1+a^2\right)\right]\left(\frac{1}{s_e} - 0.5\right) = 0. \tag{27}$$

Therefore, we could have two possible routes to satisfy the Navier–Stokes equations in the limit of $a = 1$. The first possibility is to use the condition Eq. (25) only. This condition implies that γ can be left as a free parameter so that Eq. (25) becomes a required condition between s_n and s_c. A special case is to set $s_n = s_c$, then we have

$$\frac{2-\gamma}{12} = \frac{4+\gamma}{6}, \tag{28}$$

which leads to a specific requirement that γ must to be set to -2. The second possibility to achieve the Navier–Stokes equations in the limit of $a = 1$ is to use the conditions Eqs. (23) and (24), which with $a = 1$ become

$$\frac{1}{s_e} - \frac{1}{2} = \frac{2(4+\gamma)}{(2-\gamma)}\frac{\left(\gamma+7-12c_s^2\right)}{\left(\gamma+13-12c_s^2\right)}\left(\frac{1}{s_c} - \frac{1}{2}\right) \tag{29}$$

$$\frac{1}{s_n} - \frac{1}{2} = \frac{2(4+\gamma)}{(2-\gamma)}\left(\frac{1}{s_c} - \frac{1}{2}\right). \tag{30}$$

Eq. (30) is identical to Eq. (25), but Eq. (29) imposes a condition between s_e and s_c that depends on both γ and c_s, which is really unnecessary for $a = 1$. Still, Eq. (29) indicates the limiting relationship between s_e and s_c when a is close to one, namely, on a rectangular grid, the relaxation of energy must be linked to the relaxation of cross shear stress moment. With Eqs. (23) and (24), we can show that the transport coefficients can now be simply written as

$$\nu_x = \nu + \Delta^B, \tag{31a}$$

$$\nu_y = \nu - \Delta^B, \tag{31b}$$

$$\zeta_x = \zeta - \Delta^B, \tag{31c}$$

$$\zeta_y = \zeta + \Delta^B, \tag{31d}$$

where the only remaining deviation Δ^B from isotropy is

$$\Delta^B = \frac{1-a^2}{4}\left(\frac{1}{s_e} - 0.5\right)\Delta t. \tag{32}$$

Several observations can be made. First, when $a = 1$ or when the square grid is used, the isotropy conditions are automatically satisfied and the Navier–Stokes equation is recovered. Second, when $a < 1$ and $0 < s_e < 2$, it is not possible to rigorously satisfy the Navier–Stokes equations or restore the isotropy. The bulk viscosity in the x direction is always less than that in the y direction, and the normal shear viscosity in the x direction is always larger than that in the y direction. Therefore, we have shown that Bouzidi et al.'s model does not satisfy the Navier–Stokes equations. Third, if a is close to one or if s_e is close to 2, the deviation from the Navier–Stokes equations is not significant.

2.2. The model of Zhou [17]

Next, we briefly re-visit the model proposed by Zhou [17] also intended for a rectangular grid. He simply used the transformation matrix that is identical to what is used for a square grid, namely,

$$M = \begin{pmatrix} 1 & 1 & 1 & 1 & 1 & 1 & 1 & 1 & 1 \\ -4 & -1 & -1 & -1 & -1 & 2 & 2 & 2 & 2 \\ 4 & -2 & -2 & -2 & -2 & 1 & 1 & 1 & 1 \\ 0 & 1 & 0 & -1 & 0 & 1 & -1 & -1 & 1 \\ 0 & -2 & 0 & 2 & 0 & 1 & -1 & -1 & 1 \\ 0 & 0 & 1 & 0 & -1 & 1 & 1 & -1 & -1 \\ 0 & 0 & -2 & 0 & 2 & 1 & 1 & -1 & -1 \\ 0 & 1 & -1 & 1 & -1 & 0 & 0 & 0 & 0 \\ 0 & 0 & 0 & 0 & 0 & 1 & -1 & 1 & -1 \end{pmatrix}. \tag{33}$$

This amounts to a different set of definitions for the moments. Compared with the model of Bouzidi et al. [16], energy and normal shear stress moments were defined differently in Zhou [17], while the remaining 7 moments are essentially the same up to a constant factor. In these two-dimensional moment subspace, the energy and normal stress moments between the two models can be related to each other as

$$e^B = \frac{a^2+1}{2}e^Z + \frac{1-a^2}{2}\cdot 3p_{xx}^Z, \tag{34a}$$

$$3p_{xx}^B = \frac{a^2-1}{2}e^Z + \frac{1+a^2}{2}\cdot 3p_{xx}^Z, \tag{34b}$$

where e^B, p_{xx}^B and e^Z, p_{xx}^Z refer to the energy and shear stress moments in Bouzidi's model and Zhou's model, respectively. Without the consideration of the external forcing term, the leading-order multiscaling expansion of Zhou's model leads to the following hydrodynamic equations

$$\partial_{t_1}\rho + \partial_{1x}(\rho u_x) + \partial_{1y}(\rho u_y) = 0, \tag{35a}$$

$$\partial_{t_1}(\rho u_x) + \partial_{1x}\left(\frac{2}{3}\rho + \frac{1}{6}e^{Z,(eq)} + \frac{1}{2}p_{xx}^{Z,(eq)}\right) + \partial_{1y}(\rho u_x u_y) = 0, \tag{35b}$$

$$\partial_{t_1}(\rho u_y) + \partial_{1y}\left(\frac{2a^2}{3}\rho + \frac{a^2}{6}e^{Z,(eq)} - \frac{a^2}{2}p_{xx}^{Z,(eq)}\right) + \partial_{1x}(\rho u_x u_y) = 0. \tag{35c}$$

The hydrodynamic equations at $\mathcal{O}\left(\epsilon^2\right)$ are

$$\partial_{t_2}(\rho u_x) + \partial_{1x}\left[\frac{1}{6}(1-0.5s_e)e^{Z,(1)} + \frac{1}{2}(1-0.5s_n)p_{xx}^{Z,(1)}\right] + a\partial_{1y}\left[(1-0.5s_c)p_{xy}^{Z,(1)}\right] = 0, \tag{36a}$$

$$\frac{1}{a}\partial_{t_2}(\rho u_y) + a\partial_{1y}\left[\frac{1}{6}(1-0.5s_e)e^{Z,(1)} - \frac{1}{2}(1-0.5s_n)p_{xx}^{Z,(1)}\right] + \partial_{1x}\left[(1-0.5s_c)p_{xy}^{Z,(1)}\right] = 0. \tag{36b}$$

Applying the similar inverse design analysis as done in Section 2.1, the following equilibrium moments are obtained

$$j_x^{Z,(eq)} = \rho u_x, \qquad j_y^{Z,(eq)} = \frac{\rho u_y}{a}, \tag{37a}$$

$$e^{Z,(eq)} = \rho\left[-4 + \left(6\omega a + 3u_x^2 + 6\frac{\omega}{a} + 3\frac{u_y^2}{a^2}\right)\right], \tag{37b}$$

$$p_{xx}^{Z,(eq)} = \rho\left(2\omega a + u_x^2 - \frac{2\omega}{a} - \frac{u_y^2}{a^2}\right), \tag{37c}$$

$$p_{xy}^{Z,(eq)} = \frac{\rho u_x u_y}{a}, \tag{37d}$$

$$q_x^{Z,(eq)} = \frac{1-2a^2}{a^2}\rho u_x, \tag{37e}$$

$$q_y^{Z,(eq)} = -\frac{\rho u_y}{a}, \tag{37f}$$

where ω is related to the speed of sound as $2\omega a = c_s^2$. It is noted that our inverse design analysis provides the best scenario of the model toward satisfying the correct hydrodynamics. However, the definition of $q_x^{(eq)}$ in Zhou's work is incorrect according to the requirements of self-consistency, which was set as $-\rho u_x$. While, the remaining equilibrium moments in Eq. (37) are identical to those in Zhou [17]. Substituting the above derived equilibrium moments into Eqs. (36), we obtain

$$\partial_{t_2}(\rho u_x) = \partial_{1x}\left[\rho\zeta_x^Z\left(\partial_{1x}u_x + \partial_{1y}u_y\right) + \rho\nu_x^Z\left(\partial_{1x}u_x - \partial_{1y}u_y\right)\right] + \partial_{1y}\left[\rho\nu^Z\left(\partial_{1y}u_x + \partial_{1x}u_y\right)\right], \tag{38a}$$

$$\partial_{t_2}(\rho u_y) = \partial_{1x}\left[\rho\nu^Z\left(\partial_{1y}u_x + \partial_{1x}u_y\right)\right] + \partial_{1y}\left[\rho\zeta_y^Z\left(\partial_{1x}u_x + \partial_{1y}u_y\right) + \rho\nu_y^Z\left(\partial_{1y}u_y - \partial_{1x}u_x\right)\right], \tag{38b}$$

where ζ_x^Z, ζ_y^Z, ν_x^Z and ν_y^Z are bulk and shear viscosities for x and y moment equation, respectively. Their explicit expressions are

$$\zeta_x^Z = \left(\frac{1}{s_e} - 0.5\right)\left(\frac{1}{12a^2} + \frac{7}{12} - \omega a - \frac{\omega}{a}\right)\Delta t + \left(\frac{1}{s_n} - 0.5\right)\left(\frac{\omega}{a} - \omega a + \frac{3a^2-1}{12a^2}\right)\Delta t, \tag{39a}$$

$$\zeta_y^Z = \left(\frac{1}{s_e} - 0.5\right)\left(\frac{1}{12a^2} + \frac{7}{12} - \omega a - \frac{\omega}{a}\right)\Delta t - \left(\frac{1}{s_n} - 0.5\right)\left(\frac{\omega}{a} - \omega a + \frac{3a^2-1}{12a^2}\right)\Delta t, \tag{39b}$$

$$\nu_x^Z = \frac{1}{12a^2}\left(\frac{1}{s_e} - 0.5\right)\left(1-a^2\right)\Delta t + \frac{1}{12a^2}\left(\frac{1}{s_n} - 0.5\right)\left(7a^2-1\right)\Delta t, \tag{39c}$$

$$\nu_y^Z = -\frac{1}{12a^2}\left(\frac{1}{s_e} - 0.5\right)\left(1-a^2\right)\Delta t + \frac{1}{12a^2}\left(\frac{1}{s_n} - 0.5\right)\left(7a^2-1\right)\Delta t, \tag{39d}$$

$$\nu^Z = \frac{1}{3a}\left(\frac{1}{s_c} - 0.5\right)\Delta t. \tag{39e}$$

Since the shear and bulk transfer coefficients in x and y moment are not identical, it is impossible to achieve isotropy when $a < 1$. The assumptions Zhou proposed in Eqs. (61) and (62) of his paper for the relaxation parameters also fail to satisfy the Navier–Stokes equations when $a < 1$.

If the same conditions, Eqs. (22a) and (22b), are imposed, we can obtain the following coupling relationships between the relaxation parameters

$$\frac{1}{s_e} - 0.5 = \frac{4a\left(12\omega a - 12\omega a^3 + 3a^2 - 1\right)}{\left(1-a^2\right)\left(1-7a^2\right)}\left(\frac{1}{s_c} - 0.5\right), \tag{40a}$$

$$\frac{1}{s_n} - 0.5 = \frac{4a}{7a^2-1}\left(\frac{1}{s_c} - 0.5\right). \tag{40b}$$

With these relationships, we can then express the transport coefficients

$$\nu_x^Z = \nu + \Delta^Z, \tag{41a}$$

$$\nu_y^Z = \nu - \Delta^Z, \tag{41b}$$

$$\zeta_x^Z = \zeta - \Delta^Z, \tag{41c}$$

$$\zeta_y^Z = \zeta + \Delta^Z, \tag{41d}$$

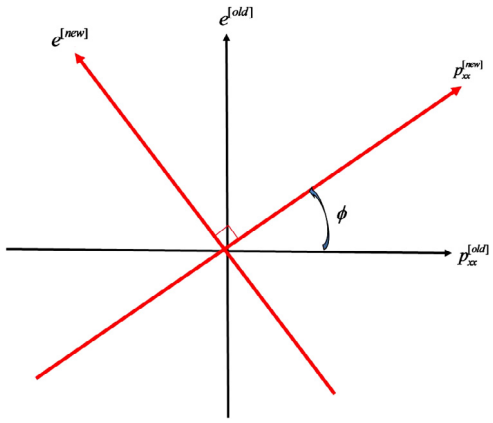

Fig. 2. Sketch of the establishing of novel MRT LBM on rectangular grid.

where the deviation from isotropy is

$$\Delta^Z = \frac{1-a^2}{12a^2}\left(\frac{1}{s_e}-0.5\right)\Delta t \tag{42}$$

and the bulk viscosity is

$$\zeta = \frac{\zeta_x+\zeta_y}{2} = \left(\frac{7}{12}+\frac{1}{12a^2}-\omega a-\frac{\omega}{a}\right)\left(\frac{1}{s_e}-0.5\right)\Delta t. \tag{43}$$

The presence of the extra term Δ^Z indicates again that it is impossible to satisfy the full isotropy conditions as required by the Navier–Stokes equations with Zhou's definitions of moments.

In summary, without introducing a new degree of freedom, it is impossible for MRT LBM to satisfy the Navier–Stokes equations when a rectangular grid is used.

3. A new MRT LBM model for a rectangular lattice grid

From the above analysis, it becomes clear that both the values and the anisotropy of the hydrodynamic transport coefficients result mainly from their dependence on the definition and relaxation parameters of energy and stress moments. Inspired by the above inverse analysis, our new rectangular MRT scheme introduces a more flexible coupling between the energy moment and normal stress moment. Specifically, we modify the definitions of these two moments by a coordinate rotation of Bouzidi et al.'s definitions, as illustrated in Fig. 2. Such rotation will not change the orthogonality property of the nine moments. The relative orientation angle becomes a new adjustable parameter.

The new energy and normal stress moments are defined in terms of Bouzidi et al.'s definitions as

$$e = e^B + \theta p_{xx}^B \tag{44a}$$

$$p_{xx} = p_{xx}^B - \theta e^B \tag{44b}$$

where $\theta \sim -\tan\phi$ with ϕ is the angle of rotation, e and p_{xx} refer to the new energy and normal viscous stress moments, respectively, while e^B and p_{xx}^B represent the corresponding moments defined in Bouzidi et al. [16] for a rectangular grid, as indicated by the transformation matrix, Eq. (4). The other 7 moments are kept the same as that defined by Bouzidi et al. [16].

With these new definitions, the second and eighth rows of the transformation matrix will be modified accordingly

$$M = \begin{pmatrix} \langle\rho| \\ \langle e| \\ \langle\varepsilon| \\ \langle j_x| \\ \langle q_x| \\ \langle j_y| \\ \langle q_y| \\ \langle 3p_n| \\ \langle p_c| \end{pmatrix} = \begin{pmatrix} 1 & 1 & 1 & 1 & 1 & 1 & 1 & 1 & 1 \\ -2R_1 & R_2 & R_3 & R_2 & R_3 & R_1 & R_1 & R_1 & R_1 \\ 4 & -2 & -2 & -2 & -2 & 1 & 1 & 1 & 1 \\ 0 & 1 & 0 & -1 & 0 & 1 & -1 & -1 & 1 \\ 0 & -2 & 0 & 2 & 0 & 1 & -1 & -1 & 1 \\ 0 & 0 & a & 0 & -a & a & a & -a & -a \\ 0 & 0 & -2a & 0 & 2a & a & a & -a & -a \\ -2R_4 & R_5 & R_6 & R_5 & R_6 & R_4 & R_4 & R_4 & R_4 \\ 0 & 0 & 0 & 0 & 0 & 1 & -1 & 1 & -1 \end{pmatrix} \tag{45}$$

where $R_1 = r_1 + \theta r_4$, $R_2 = r_2 + \theta r_5$, $R_3 = r_3 + \theta r_6$, $R_4 = r_4 - \theta r_1$, $R_5 = r_5 - \theta r_2$, $R_6 = r_6 - \theta r_3$, and $r_1, r_2, r_3, r_4, r_5, r_6$ have been defined previously in Section 2.

By the same inverse design process using the Chapman–Enskog analysis presented in Section 2.1, it is found that two equilibrium moments (*i.e.*, energy and normal viscous stress) are modified and the others are the same as in Section 2.1. The updated equilibrium moments are

$$\mathbf{m}^{(eq)} = \rho \begin{bmatrix} 1 \\ 2\left(3c_s^2 - r_1\right) + 3\left(u_x^2 + u_y^2\right) + \theta\left[\dfrac{r_4}{a^2}\left(3r_1c_s^2 - 2a^2\right) + 3\left(a^2u_x^2 - \dfrac{u_y^2}{a^2}\right)\right] \\ \alpha + \beta u^2 \\ u_x \\ \dfrac{\gamma - 4r_4}{2a^2}u_x \\ u_y \\ \dfrac{\gamma}{2}u_y \\ \dfrac{r_4}{a^2}\left(3r_1c_s^2 - 2a^2\right) + 3\left(a^2u_x^2 - \dfrac{u_y^2}{a^2}\right) - \theta\left[2\left(3c_s^2 - r_1\right) + 3(u_x^2 + u_y^2)\right] \\ \dfrac{u_xu_y}{a} \end{bmatrix}. \tag{46}$$

The macroscopic equations for the new MRT scheme are structurally identical to that of those given in Section 2.1. The Euler equations are satisfied at $\mathcal{O}(\epsilon)$. The explicit expressions at $\mathcal{O}(\epsilon^2)$ are as follows:

$$\partial_{t_2}\rho = 0, \tag{47a}$$

$$\partial_{t_2}\left(\rho u_x\right) = -\frac{(a^2-\theta)(1-0.5s_n)}{3(a^4+1)(\theta^2+1)}\partial_{1x}p_{xx}^{(1)} - a(1-0.5s_c)\partial_{1y}p_{xy}^{(1)} - \frac{(\theta a^2+1)(1-0.5s_e)}{3(a^4+1)(\theta^2+1)}\partial_{1x}e^{(1)}, \tag{47b}$$

$$\partial_{t_2}\left(\rho u_y\right) = \frac{a^2(\theta a^2+1)(1-0.5s_n)}{3(a^4+1)(\theta^2+1)}\partial_{1y}p_{xx}^{(1)} - a(1-0.5s_c)\partial_{1x}p_{xy}^{(1)} - \frac{a^2(a^2-\theta)(1-0.5s_e)}{3(a^4+1)(\theta^2+1)}\partial_{1y}e^{(1)}. \tag{47c}$$

It follows that the transport coefficients resulting from the $\mathcal{O}(\epsilon^2)$ analysis, as defined in Eqs. (15a) and (15b), are

$$\begin{aligned} \nu_x &= \frac{\Delta t}{6\left(a^4+1\right)}\left(3 + a^2 - \frac{\gamma}{2a^2} - \frac{a^2\gamma}{2} - \frac{2}{a^2}\right)\left[\left(\frac{1}{s_n} - 0.5\right)\frac{a^2-\theta}{\theta^2+1} + \left(\frac{1}{s_e} - 0.5\right)\frac{\theta(\theta a^2+1)}{\theta^2+1}\right] \\ &\quad + \frac{\Delta t}{2(a^4+1)}(1-a^2)\left[\left(\frac{1}{s_e} - 0.5\right)\frac{\theta a^2+1}{\theta^2+1} - \theta\left(\frac{1}{s_n} - 0.5\right)\frac{a^2-\theta}{\theta^2+1}\right], \end{aligned} \tag{48a}$$

$$\begin{aligned} \nu_y &= \frac{a^2\Delta t}{6(a^4+1)}\left(3 + a^2 - \frac{\gamma}{2a^2} - \frac{a^2\gamma}{2} - \frac{2}{a^2}\right)\left[\left(\frac{1}{s_n} - 0.5\right)\frac{\theta a^2+1}{\theta^2+1} - \theta\left(\frac{1}{s_e} - 0.5\right)\frac{(a^2-\theta)}{\theta^2+1}\right] \\ &\quad + \frac{a^4\Delta t}{2(a^4+1)}(a^2-1)\left[\left(\frac{1}{s_e} - 0.5\right)\frac{a^2-\theta}{a^2\left(\theta^2+1\right)} + \theta\left(\frac{1}{s_n} - 0.5\right)\frac{\theta a^2+1}{a^2(\theta^2+1)}\right], \end{aligned} \tag{48b}$$

$$\begin{aligned} \zeta_x &= \frac{\Delta t}{6(a^4+1)}\left(7 + \gamma + 3a^2 - 12c_s^2\right)\left[\left(\frac{1}{s_e} - 0.5\right)\frac{\theta a^2+1}{\theta^2+1} - \theta\left(\frac{1}{s_n} - 0.5\right)\frac{a^2-\theta}{\theta^2+1}\right] \\ &\quad + \frac{\Delta t}{6(a^4+1)}\left(5a^2 - \frac{2}{a^2} - 3 - \frac{\gamma}{2a^2} - 6a^2c_s^2 + 6\frac{c_s^2}{a^2} + \frac{a^2\gamma}{2}\right) \\ &\quad \times \left[\left(\frac{1}{s_n} - 0.5\right)\frac{a^2-\theta}{\theta^2+1} + \theta\left(\frac{1}{s_e} - 0.5\right)\frac{\theta a^2+1}{\theta^2+1}\right], \end{aligned} \tag{48c}$$

$$\begin{aligned} \zeta_y &= \frac{a^4\Delta t}{6(a^4+1)}(7 + \gamma + 3a^2 - 12c_s^2)\left[\left(\frac{1}{s_n} - 0.5\right)\frac{\theta(\theta a^2+1)}{a^2(\theta^2+1)} + \left(\frac{1}{s_e} - 0.5\right)\frac{a^2-\theta}{a^2(\theta^2+1)}\right] \\ &\quad + \frac{a^2\Delta t}{6(a^4+1)}\left(-5a^2 + \frac{2}{a^2} + 3 + \frac{\gamma}{2a^2} + 6a^2c_s^2 - 6\frac{c_s^2}{a^2} - \frac{a^2\gamma}{2}\right) \\ &\quad \times \left[\left(\frac{1}{s_n} - 0.5\right)\frac{\theta a^2+1}{\theta^2+1} - \theta\left(\frac{1}{s_e} - 0.5\right)\frac{a^2-\theta}{\theta^2+1}\right], \end{aligned} \tag{48d}$$

$$\nu = \frac{\gamma+4}{6}\left(\frac{1}{s_c} - 0.5\right)\Delta t. \tag{48e}$$

At this moment, they look rather complicated. Clearly, when $\theta = 0$, Eqs. 48(a–e) reduce to Eqs. 20(a–e) as expected. We adopt the same procedure by first imposing part of the isotropy requirements, given by Eqs. (22a) and (22b). The following coupling relationships can then be derived,

$$\left(\frac{1}{s_e} - 0.5\right) = \frac{2(\gamma+4)(a^4+1)(1+\theta^2)C_{22}}{C_{11}C_{22} - C_{12}C_{21}}\left(\frac{1}{s_c} - 0.5\right) \tag{49a}$$

$$\left(\frac{1}{s_n} - 0.5\right) = -\frac{2(\gamma+4)(a^4+1)(1+\theta^2)C_{21}}{C_{11}C_{22} - C_{12}C_{21}}\left(\frac{1}{s_c} - 0.5\right) \tag{49b}$$

where

$$\begin{aligned}
C_{11} &= \left(3 + a^2 - \frac{\gamma}{2a^2} - \frac{a^2\gamma}{2} - \frac{2}{a^2}\right)(2\theta^2a^2 + \theta - a^4\theta) + 3(1-a^2)(2\theta a^2 + 1 - a^4),\\
C_{12} &= \left(3 + a^2 - \frac{\gamma}{2a^2} - \frac{a^2\gamma}{2} - \frac{2}{a^2}\right)(2a^2 - \theta + a^4\theta) + 3(1-a^2)(\theta^2 - 2a^2\theta - a^4\theta^2),\\
C_{21} &= 2a^2\theta\left(7 + \gamma + 3a^2 - 12c_s^2\right) + (1-a^4)(7+\gamma+3a^2-12c_s^2) + (a^4+1)\left(3 + a^2 - \frac{\gamma}{2a^2} - \frac{a^2\gamma}{2} - \frac{2}{a^2}\right)\theta\\
&\quad + 3(a^4+1)(1-a^2) + (1-a^4)(1-a^2)\left[-\frac{2}{a^2} - 5 + \left(6c_s^2 - \frac{\gamma}{2}\right)\left(1 + \frac{1}{a^2}\right)\right]\theta\\
&\quad + (1-a^2)\left[\left(12c_s^2 - \gamma - 4\right)\left(1+a^2\right) - 6a^2\right]\theta^2,\\
C_{22} &= -2a^2\theta\left(7 + \gamma + 3a^2 - 12c_s^2\right) + (1-a^4)(7+\gamma+3a^2-12c_s^2)\theta^2\\
&\quad - (a^4+1)\left(3 + a^2 - \frac{\gamma}{2a^2} - \frac{a^2\gamma}{2} - \frac{2}{a^2}\right)\theta + 3(a^4+1)(1-a^2)\theta^2 - (1-a^4)(1-a^2)\\
&\quad \times\left[-\frac{2}{a^2} - 5 + \left(6c_s^2 - \frac{\gamma}{2}\right)\left(1 + \frac{1}{a^2}\right)\right]\theta + (1-a^2)\left[(12c_s^2 - \gamma - 4)(1+a^2) - 6a^2\right].
\end{aligned}$$

It is important to note that the coefficients C_{11}, C_{12}, C_{21}, and C_{22} are functions of a, c_s, γ, θ only; they do not depend on the relaxation parameters. When $\theta = 0$, the coupling relationships in Eqs. 48(a–b) reduce precisely to the coupling relationships Eqs. (23) and (24). Furthermore, with the above conditions, the transport coefficients can now be rewritten in the similar way as in Eqs. (25) and (34) as

$$\nu_x = \nu + \frac{\nu_x - \nu_y}{2} \tag{50a}$$

$$\nu_y = \nu - \frac{\nu_x - \nu_y}{2} \tag{50b}$$

$$\zeta_x = \zeta - \frac{\nu_x - \nu_y}{2} \tag{50c}$$

$$\zeta_y = \zeta + \frac{\nu_x - \nu_y}{2} \tag{50d}$$

where

$$\frac{\nu_x - \nu_y}{2} = \frac{\theta\Delta t}{12\left(1+\theta^2\right)}\left(3 + a^2 - \frac{\gamma}{2a^2} - \frac{a^2\gamma}{2} - \frac{2}{a^2}\right)\left(\frac{1}{s_e} - \frac{1}{s_n}\right) + \frac{(1-a^2)\Delta t}{4\left(1+\theta^2\right)}\left[\left(\frac{1}{s_e} - 0.5\right) + \theta^2\left(\frac{1}{s_n} - 0.5\right)\right]. \tag{51}$$

Now the final condition for matching the Navier–Stokes equations is simply to require

$$\frac{\nu_x - \nu_y}{2} = 0 \tag{52}$$

which leads to

$$\left(3 + a^2 - \frac{\gamma}{2a^2} - \frac{a^2\gamma}{2} - \frac{2}{a^2}\right)\left[\theta\left(\frac{1}{s_e} - \frac{1}{s_n}\right)\right] + 3(1-a^2)\left[\left(\frac{1}{s_e} - 0.5\right) + \theta^2\left(\frac{1}{s_n} - 0.5\right)\right] = 0. \tag{53}$$

Now recall Eq. (49), which states the coupling relationship: $(s_e^{-1} - 0.5) \sim (s_c^{-1} - 0.5)$ and $(s_n^{-1} - 0.5) \sim (s_c^{-1} - 0.5)$. This implied that all the relaxation parameters s_e, s_n, s_c can be removed from Eq. (53) if we substitute Eqs. (49) into it. The relationship between a, c_s, γ, θ is

$$\left(3 + a^2 - \frac{\gamma}{2a^2} - \frac{a^2\gamma}{2} - \frac{2}{a^2}\right)(C_{21} + C_{22})\theta + 3(1-\theta^2)(C_{22} - C_{21}\theta^2) = 0. \tag{54}$$

Substituting the expressions of C_{11}, C_{12}, C_{21}, and C_{22}, we can rewrite Eq. (53) in the following form

$$(1-a^2)\left(1+\theta^2\right)\left(A\theta^2+B\theta-A\right)=0, \tag{55}$$

where

$$A=3(a^2-1)\left[(\gamma-12c_s^2)(1+a^2)+2(5a^2+2)\right],$$

$$B=a^2(12\gamma-108c_s^2+66)+18a^6(c_s^2-1)+18\frac{c_s^2}{a^2}+18(a^4-1).$$

Several interesting observations are now in order. First, in the limit of $a\to 1$, Eq. (55) is automatically satisfied for any θ. Namely, the Navier–Stokes equations emerge. In this limit, any value of θ would work, with the formulation of Bouzidi et al. [16] and Zhou [17] as two special examples. In this limit, the coupling relationships, Eqs. (49a–b), are not related with θ and become $s_e=s_n=s_c$. Second, when $a\neq 1$, then we must require

$$A\theta^2+B\theta-A=0, \tag{56}$$

which is a surprising simple second-order equation for setting θ in terms of a, c_s, and γ, so that the full isotropy can be realized on a rectangular grid to yield the Navier–Stokes equations. This equation has two solutions θ_1 and $\theta_2=-1/\theta_1$. The relationship $\theta_2=-1/\theta_1$ stems from the fact that the last coefficient $(-A)$ differs from the first coefficient (A) by a sign. The second solution θ_2 represents the result of rotating the direction of the $e-p_{xx}$ axes in the first solution by 90°. Therefore, without the loss of generality, we may restrict our discussions below to only the solution of $\theta>0$, which is given as

$$\theta_1=-\frac{B}{2A}+\frac{\sqrt{4A^2+B^2}}{2A}. \tag{57}$$

The above analysis indicates that the free parameter θ provides the feasibility to eliminate the anisotropy in the transport coefficients. Such feasibility does not exist in the models of Bouzidi et al. [16] and Zhou [17], which is the reason why their models fail to rigorously satisfy the Navier–Stokes equations. We have derived the explicit requirement for setting this parameter in terms of the model parameters c_s, γ, a. Under this condition, Eq. (47) can be inverted to express the macroscopic stress components in terms of the mesoscopic non-equilibrium moments as

$$\frac{1}{\rho_0}\tau_{xy}\equiv\nu\left(\frac{\partial u_x}{\partial y}+\frac{\partial u_y}{\partial x}\right)=-a\,(1-0.5s_c)\,p_{xy}^{(1)} \tag{58a}$$

$$\frac{1}{\rho_0}\tau_{xx}=-\frac{1}{\rho_0}\tau_{yy}\equiv\nu\left(\frac{\partial u_x}{\partial x}-\frac{\partial u_y}{\partial y}\right)=\frac{(-2a^2+\theta-\theta a^4)(1-0.5s_n)}{6(1+a^4)(1+\theta^2)}p_{xx}^{(1)}+\frac{(-2\theta a^2-1+a^4)(1-0.5s_e)}{6(1+a^4)(1+\theta^2)}e^{(1)} \tag{58b}$$

$$\frac{1}{\rho_0}\tau_{xx}^{V}=\frac{1}{\rho_0}\tau_{yy}^{V}\equiv\zeta\left(\frac{\partial u_x}{\partial x}-\frac{\partial u_y}{\partial y}\right)=\frac{\theta(1-0.5s_n)}{6(1+\theta^2)}p_{xx}^{(1)}-\frac{(1-0.5s_e)}{6(1+\theta^2)}e^{(1)}. \tag{58c}$$

We stress that, in principle, for a given lattice aspect ratio a, c_s and γ are two free parameters in the model, which can be tuned to achieve the best numerical stability of our proposed MRT LBM model on a rectangular grid.

4. Numerical validations

We shall now confirm our new MRT LBM scheme on a rectangular grid, by considering two flow problems: a 2D channel flow and a 2D lid-driven cavity flow. For a given value of $a\neq 1$, the values of the model parameters should be chosen to keep the simulation numerically stable. The range of the relaxation parameters should be $0<s_i<2$. Here we consider steady-state flows. The simulation ends when the following condition

$$Err=\sqrt{\frac{\sum_{i,j}[u_x(i,j,t+dt)-u_x(i,j,t)]^2+[u_y(i,j,t+dt)-u_y(i,j,t)]^2}{\sum_{i,j}[u_x(i,j)^2+u_y(i,j)^2]}}<10^{-8} \tag{59}$$

is reached.

4.1. The 2D channel flow

In these cases, the numerical simulations are conducted by the new MRT LBM model with several different values of the grid aspect ratio a and the results are compared with the exact solution. The periodic boundary conditions are applied to the flow inlet and outlet, the half-way bounce back conditions are imposed on the channel walls. The model parameters are listed in Table 1. Note that the value of θ is determined from Eq. (56) after c_s and γ are chosen. The relaxation parameter s_c

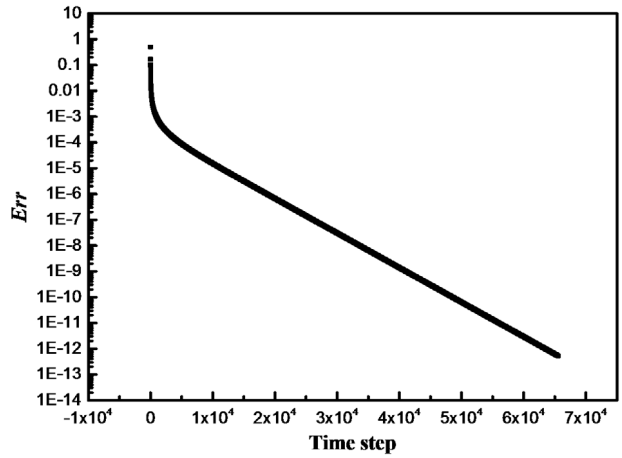

Fig. 3. The relative difference of the maximum velocity at $x/L = 0.5$ between two adjacent time steps.

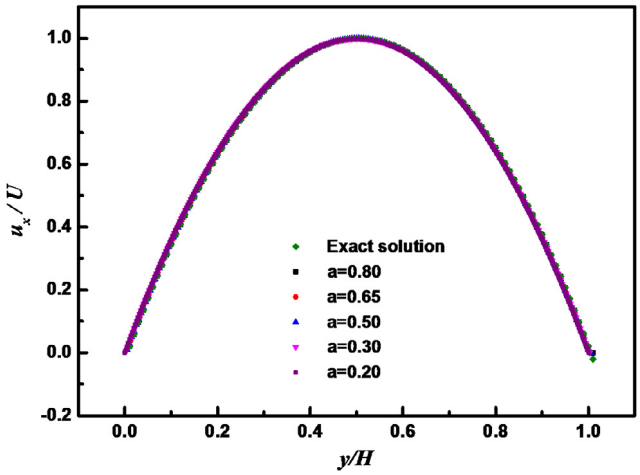

Fig. 4. Velocity profiles obtained with different grid aspect ratios.

Table 1
Summary of the model parameters used for the 2D channel flow simulations.

a	γ	c_s^2	$Nx \times Ny$	θ	s_c	s_e	s_n	Viscosity
0.80	−2.3	0.3333	4×125	0.0261	1.1724	1.8877	1.0665	0.10
0.65	−2.0	0.3333	4×154	0.4215	1.2500	1.2508	0.3652	0.10
0.50	−3.0	0.16	4×200	0.2977	0.9091	1.2859	0.3155	0.10
0.30	−3.8	0.04	4×334	0.0757	0.7143	1.8091	0.6504	0.03
0.20	−3.9	0.01	4×500	0.0494	0.4348	1.7394	0.3214	0.03

is chosen according to the set-up of the flow problem, and s_e and s_n are obtained by Eqs. (49a–b). Besides, for all the cases studied here, the relaxation times s_ρ, s_j are set to be 0, the other two relaxation times are chosen to be $s_\varepsilon = 1.4$, $s_q = 1.5$.

Fig. 3 shows the time evolution of the relative difference of the maximum velocity between two adjacent time steps at $x/L = 0.5$, where L is the channel length. The relative difference decreases monotonically in time, showing that the flow has reached the steady state. Only the simulated, steady-state velocity distribution is discussed next. Fig. 4 shows the dimensionless velocity profiles (normalized by the channel center velocity) for 5 different values of the grid aspect ratio a, as well as the theoretical velocity profile. We observe that the results from our new model are in excellent agreement with the exact solution. It also should be noted here that extremely smaller grid ratio will lead to numerical instability.

Next, in Fig. 5, we compare the relative errors between the computed and exact results at different resolutions (N_y) in the y direction for $a = 0.8, 0.5, 0.3$ and $a = 0.2$, in which the Reynolds number varies with the resolutions and viscosity remains the same. The relative error is employed for comparison and defined as: $(u_{x,simulated} - u_{x,theory})/U$ at $x/L = 0.5$, where $u_{x,theory}$ is the theoretical velocity of the Poiseuille flow. The two dash-dotted lines denote the slope of -2. Clearly, it proves the new scheme is of second-order accuracy for $a = 0.8$ though the error seems to be larger if a smaller a is used. It

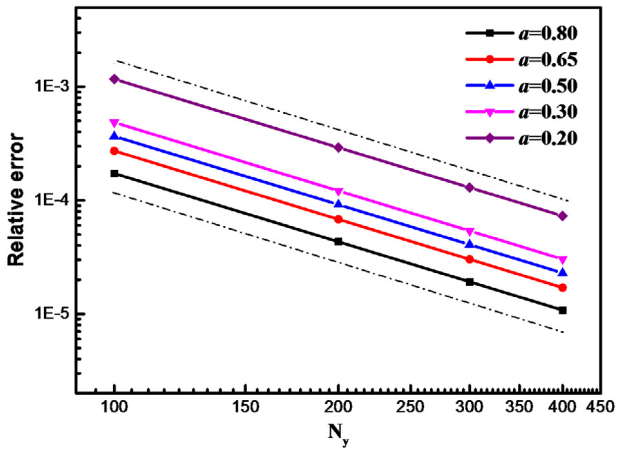

Fig. 5. The relative error between the simulated results and the exact resolution at the steady state.

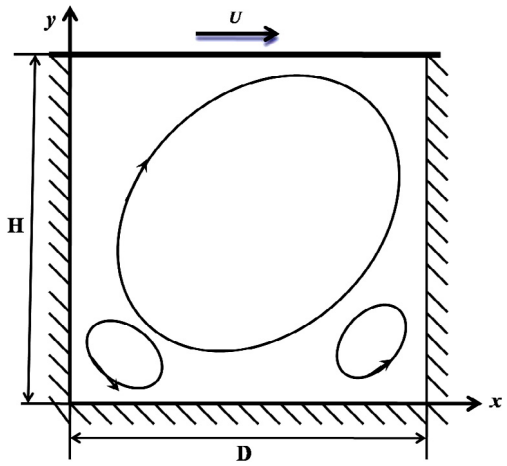

Fig. 6. A schematic of lid-driven cavity flow in a square cavity.

is well known that mid-way bounce back boundary results to the second-order accuracy for standard LBM models [22,23]. Here we confirm that the same is true on a rectangular grid.

4.2. The 2D lid-driven cavity flow

The 2D lid-driven cavity flow (Fig. 6) has been studied as a standard benchmark case to test many numerical methods, in which D, H are the width and height of the cavity, respectively. Depending on the flow Reynolds number, the flow pattern and the number of corner vortices are different. This flow has also been extensively used to study the performance of LBM solutions [24–26]. We consider a square cavity of width H. At the top boundary, $u_y = 0$ and $u_x = U$. Since the equilibrium distributions depend on a, we need to obtain $\mathbf{f}^{(eq)}$ from $\mathbf{m}^{(eq)}$ by $\mathbf{f}^{(eq)} = M^{-1}\mathbf{m}^{(eq)}$. The lattice node is placed half-way from the top wall, and the bounce back on the top wall is implemented as

$$f_4(\mathbf{x}_f, t + \Delta t) = \tilde{f}_2(\mathbf{x}_f, t) - \left[f_2^{(eq)} - f_4^{(eq)}\right] = \tilde{f}_2(\mathbf{x}_f, t)$$

$$f_7(\mathbf{x}_f, t + \Delta t) = \tilde{f}_5(\mathbf{x}_f, t) - \left[f_5^{(eq)} - f_7^{(eq)}\right] = \tilde{f}_5(\mathbf{x}_f, t) - \rho\frac{(\gamma + 4)}{12a^2}U$$

$$f_8(\mathbf{x}_f, t + \Delta t) = \tilde{f}_6(\mathbf{x}_f, t) - \left[f_6^{(eq)} - f_8^{(eq)}\right] = \tilde{f}_6(\mathbf{x}_f, t) + \rho\frac{(\gamma + 4)}{12a^2}U$$

where the nearly incompressible formulation is used, with $\rho = \rho_0 + \delta\rho$ and $\rho_0 = 1$. Note that the above half-way bounce-back relations for a moving wall reduce to the standard forms when $a = 1$ and $\gamma = -2$. The value of ρ in the above is simply set to ρ_0. On the other three walls, the half-way bounce back scheme is applied. The governing parameter of the flow is the Reynolds number defined as $Re = UH/\nu$. The number of lattice nodes in x direction is fixed to 100 and that in y direction is adjusted according to different grid aspect ratios a.

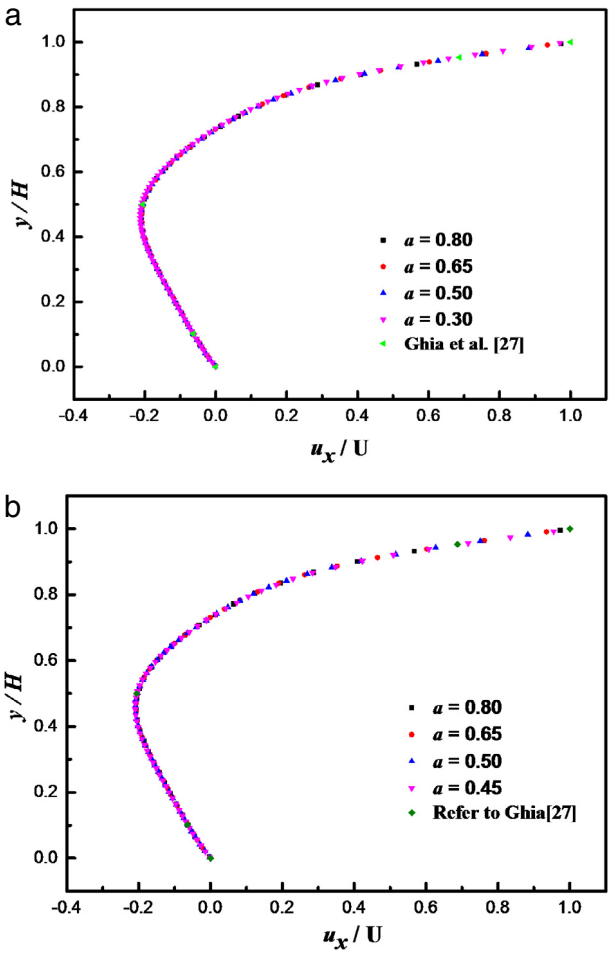

Fig. 7. Comparison of u_x at the mid-plane with Re $= 100$. (a) Our new model; (b) Bouzidi et al.'s scheme.

In Figs. 7 and 8, we show the steady-state velocity profiles at $x/D = 0.5$ and $y/H = 0.5$ respectively, using both our new model and the model of Bouzidi et al., for the cavity flow at $Re = 100$. The computational parameters for the former are listed in Table 2. For the latter case the parameters are listed in Table 3 which are taken from Table 4.1 in Bouzidi et al. [16] and the coupled relaxation times are obtained from Eqs. (23) and (24). The other relaxation times are set as: $s_\rho = 0$, $s_\varepsilon = 1.4$, $s_j = 0$, $s_q = 1.5$. The results from a previous study [27] are also shown for comparison which employed the multigrid procedure and finite-difference solution.

In Figs. 7(a) and 8(a), the steady-state u_x and u_y velocity profiles along the centerline from our new model for four different values of a are plotted. The smallest a is 0.3 and the new model is still numerically stable. These clearly demonstrate that the results are not affected by a and are in excellent agreement with the work of Ghia et al. [27]. The corresponding results for the model of Bouzidi et al. [16] are shown in Figs. 7(b) and 8(b). The code based on their model became unstable at $a = 0.3$, so no results for $a = 0.3$ are shown. Interesting, for $a \geq 0.5$, their results are also in good agreement with one another and with those of Ghia et al. [27], although a closer inspection shows some minor differences in the u_y profiles. The good agreement for the model of Bouzidi et al. [16] is somewhat coincidental, which can be explained by the deviation term of the transport coefficients in Eq. (32). When $a = 0.8$ and $Re = 100$, this departure is around 0.015, which is significantly less than the shear viscosity $\nu = 0.1$. For $a = 0.5$, the departure term is 0.056, again is relatively small when compared to $\nu = 0.1$. It also found Δ^B should be less than a certain value in order to keep the numerical stability and accuracy, otherwise the computation by the Bouzidi et al. scheme will be unstable. Further study is needed to investigate the effect of the departure term on the simulation.

Moreover, the computations based on Bouzidi's scheme were found to be unstable when the Reynolds number is higher. Our model, on the other hand, remains stable. Fig. 9 shows velocity profiles at $x/H = 0.5$ and $a = 0.8$ with different flow Reynolds numbers. The parameters are listed in Table 2. In general, the agreement for the new model is good at most of the flow Reynold numbers, except at $Re = 3200$, which may be due to the low resolution adopted in the simulation. For the scheme of Bouzidi et al., the computation became unstable when $Re > 1000$. These tests show that the new model with the additional parameter θ can improve numerical stability, in addition to rigorous consistency with the Navier–Stokes

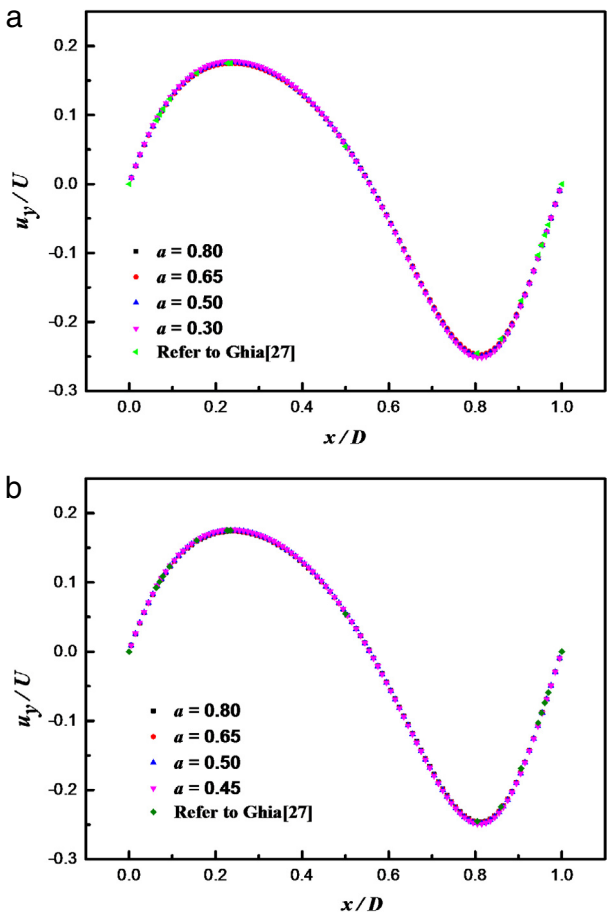

Fig. 8. Comparison of u_y at the mid-plane with Re = 100. (a) Our new model; (b) Bouzidi et al.'s scheme.

Table 2
Summary of the computational parameters for the updated MRT scheme on rectangular grid.

a	γ	c_s^2	θ	Re	s_c	s_e	s_n	U	$Nx \times Ny$	Viscosity
0.80	−2.3	0.3333	0.0261	100	1.1724	1.8878	1.0665	0.1	100 × 125	0.10
0.65	−2.0	0.3333	0.4215	100	1.2500	1.2508	0.3652	0.1	100 × 154	0.10
0.50	−3.0	0.16	0.2977	100	0.9091	1.2859	0.3155	0.1	100 × 200	0.10
0.30	−3.8	0.04	0.0757	100	0.7143	1.8091	0.6504	0.03	100 × 334	0.03
0.80	−2.3	0.16	1.5549	400	1.6749	1.6747	1.3063	0.11	100 × 125	0.02750
0.80	−2.3	0.16	1.5549	1000	1.8559	1.8558	1.6496	0.11	100 × 125	0.01100
0.80	−1.7	0.16	2.1351	3200	1.9870	1.9774	1.4218	0.04	100 × 125	0.00125

Table 3
Summary of the computational parameters for Bouzidi et al.'s scheme [16].

a	γ	c_s^2	s_c	s_e	s_n	Δ^B
0.80	−0.90	0.3398	1.4419	1.4889	0.7572	0.015
0.65	−1.70	0.2267	1.3143	1.3278	0.5963	0.036
0.50	−2.55	0.1421	1.0943	1.2498	0.4132	0.056

equation. A full discussion of the optimization of the model parameters and their impact on numerical stability is beyond the scope of the current paper, and will be reported in a separate paper.

In Fig. 10, we plot the velocity contours and streamlines for the cavity flows at four different Reynolds numbers by the new model. The structure of the flow depends on the flow Reynolds number. With increasing flow Reynolds number, the primary vortex moves toward the left and downward gradually and becomes increasing circular. The size, number, and intensity of the corner vortices all increase with *Re*. The secondary corner eddies appear initially near the corners. Their centers move slowly toward the cavity center with the increase of Reynolds number. Finally, in Fig. 11 we compare the

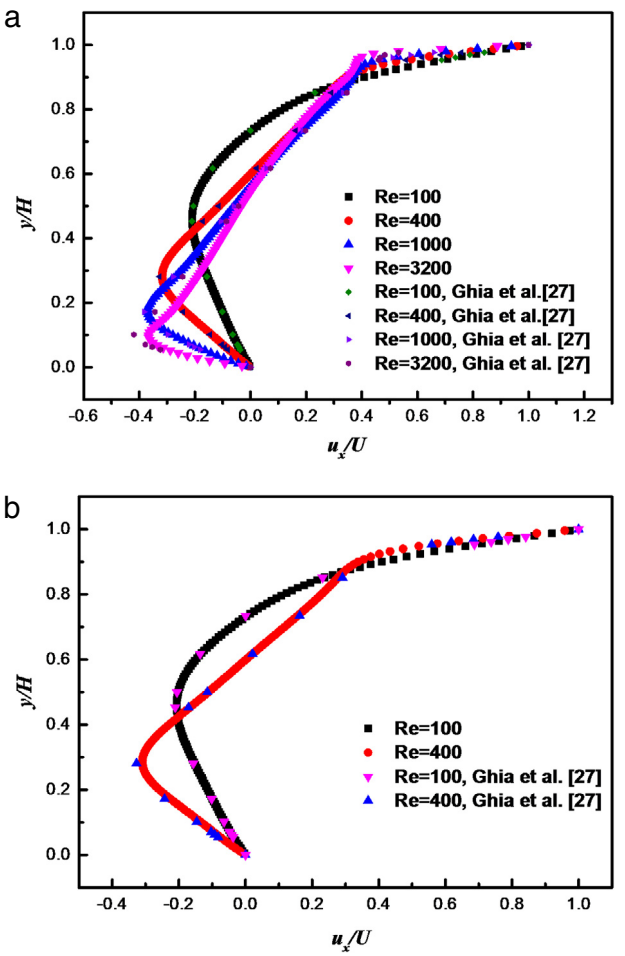

Fig. 9. Comparison of u_x at the mid-plane with different Reynolds number. (a) New model; (b) Bouzidi et al.'s scheme.

locations of the primary vortex center at different Reynolds numbers against the data from Ghia et al. [27]. The agreement is satisfactory. These tests validate our new model on a rectangular grid, in terms of both accuracy and numerical stability.

4.3. 2D Taylor–Green vortex flow

In order to further probe the isotropy of the new MRT model, a two-dimensional (2D) decaying Taylor–Green vortex flow is considered here, which was adopted to probe the anisotropy of Zhou's model [17] by Chikatamarla [28]. This flow has an analytical solution of the incompressible Navier–Stokes equation, residing in a domain of size $L_x \times L_y$. The velocity and pressure fields are

$$u_x(x, y, t) = -U_0 \cos(k_x x) \sin(k_y y) e^{-k^2 \nu t}, \tag{60a}$$

$$u_y(x, y, t) = \frac{k_x}{k_y} U_0 \sin(k_x x) \cos(k_y y) e^{-k^2 \nu t}, \tag{60b}$$

$$p(x, y, t) = -\frac{1}{4} \rho U_0^2 \left[\cos(2k_x x) + \left(\frac{k_x}{k_y} \right)^2 \cos(2k_y y) \right] e^{-2k^2 \nu t} + P_0 \tag{60c}$$

where U_0 is the initial velocity amplitude, ν is the shear viscosity, $k_x = 2\pi / L_x$ and $k_y = 2\pi / L_y$ are the wave numbers in x and y directions, respectively, $k = \sqrt{k_x^2 + k_y^2}$ and P_0 is the mean reference pressure.

The analytical solutions of the stress components can be obtained from Eq. (59), which are given here

$$\tau_{xx} = \rho \nu \left(\frac{\partial u_x}{\partial x} - \frac{\partial u_y}{\partial y} \right) = 4\pi \rho \nu \frac{U_0}{L_x} \sin \left(\frac{2\pi x}{L_x} \right) \sin \left(\frac{2\pi y}{L_y} \right) e^{-k^2 \nu t},$$

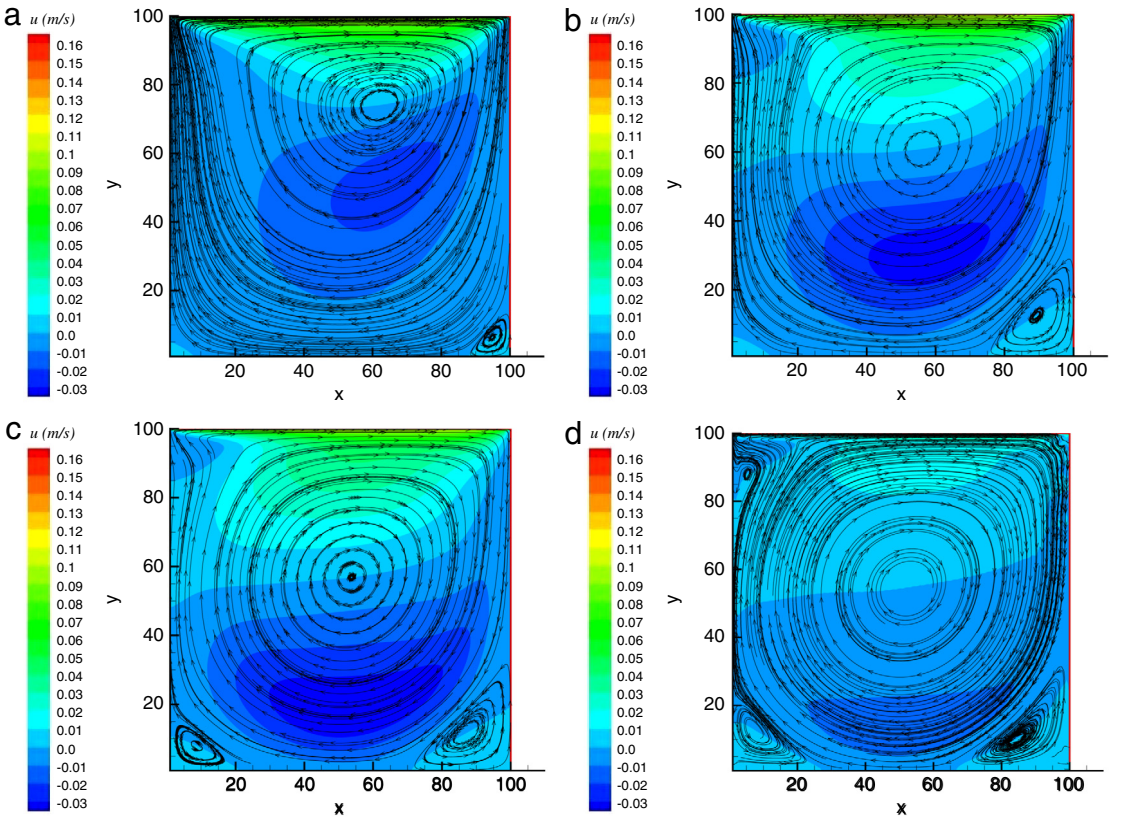

Fig. 10. Velocity contour and streamlines for the flows with different Reynolds numbers. (a) $Re = 100$, (b) $Re = 400$, (c) $Re = 1000$, (d) $Re = 3200$.

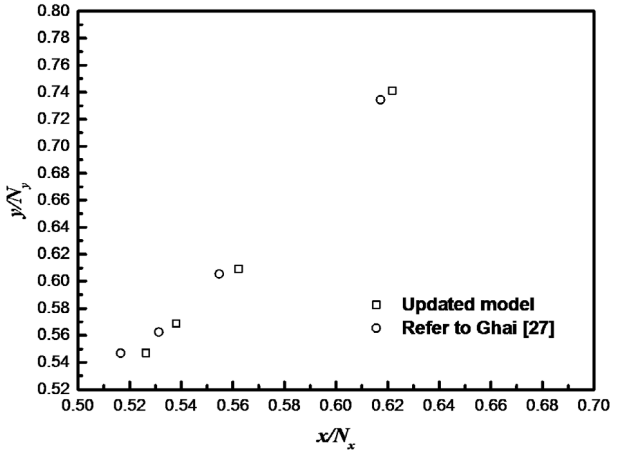

Fig. 11. Comparison of the primary vortex location at different Reynolds numbers.

$$\tau_{xy} = \rho\nu\left(\frac{\partial u_x}{\partial y} + \frac{\partial u_y}{\partial x}\right) = 2\pi\rho\nu\frac{U_0}{L_x}\frac{L_y}{L_x}\left[1 - \left(\frac{L_x}{L_y}\right)^2\right]\cos\left(\frac{2\pi x}{L_x}\right)\cos\left(\frac{2\pi y}{L_y}\right)e^{-k^2\nu t},$$

$$\tau_{yy} = \rho\nu\left(\frac{\partial u_y}{\partial y} - \frac{\partial u_x}{\partial x}\right) = -\tau_{xx}.$$

Since the velocity field of the Taylor–Green vortex flow is divergence-free, it follows that the bulk stress $\tau^V_{xx} = \tau^V_{yy} = \rho\zeta\left(\frac{\partial u_x}{\partial x} + \frac{\partial u_y}{\partial y}\right) = 0$.

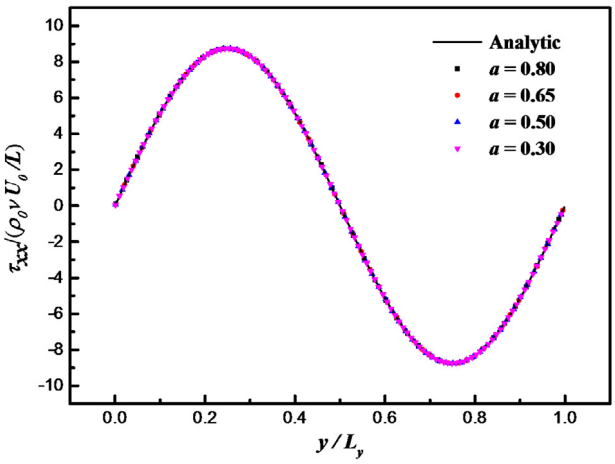

Fig. 12. The converged normal stress ($\tau_{xx}/\rho_0 U_0^2$) profiles at $t = 0$ by the iterative approach for the Taylor–Green vortex flow, obtained with different a values, are compared to the analytical curve.

Table 4
Summary of the model parameters used for the 2D Taylor–Green vortex flow.

a	γ	c_s^2	$Nx \times Ny$	θ	s_c	s_e	s_n	Re	u_0
0.80	−2.0	0.3333	200 × 250	0.6400	1.9084	1.9084	1.8110	100	0.100
0.65	−2.0	0.3333	200 × 308	0.4225	0.9091	0.9091	0.2006	100	0.100
0.50	−3.1	0.09	200 × 400	0.4070	1.5789	1.7567	0.9494	100	0.010
0.30	−3.7	0.04	200 × 666	0.1115	1.5151	1.9208	1.0890	100	0.004

Here we consider the special case of $k_x = k_y = 2\pi/L$ and set $P_0 = 0$. The Reynolds number is defined as $Re = \rho L u_0/\nu$. The flow is then isotropic and the average kinetic energy in the x-direction is identical to that in the y-direction, which is given as

$$\frac{1}{2}\left\langle u_x^2(x,y,t)\right\rangle = \frac{1}{2}\left\langle u_y^2(x,y,t)\right\rangle = \frac{1}{8}U_0^2 e^{-2k^2\nu t}. \tag{61}$$

Here the angle brackets denote spatial average at a given time. We shall define the corresponding normalized quantities as $K_x = 4\left\langle u_x^2(x,y,t)\right\rangle/U_0^2$ and $K_y = 4\left\langle u_y^2(x,y,t)\right\rangle/U_0^2$, and theoretically they both vary in time as $e^{-2k^2\nu t}$. The computed ratio of $\langle K_x\rangle / \langle K_y\rangle$ from a LBM model may be compared to the analytical value of one, as a check whether the physical isotropy of the flow is satisfied.

In our LBM simulations, the periodic boundary conditions are applied to both directions. The computational parameters are given in Table 4. The initial condition for the distribution functions must be specified properly. There are two general methods to specific the correct initial condition. The first method is to describe both equilibrium moments and non-equilibrium moments according to the results from the Chapman–Enskog analysis, here only the non-equilibrium moments for e, p_{xx}, and p_{xy} are relevant according to Eqs. (47) and (58). The moments are then inverted to obtain the distribution functions f_i at $t = 0$. Alternatively, we can use iterations to converge the initial non-equilibrium moments after the equilibrium moments are constrained by the velocity and pressure fields. Clearly, the first method is preferred. Fig. 12 shows the results of converged normal stress by the iterative method for different a, along with the analytical solution. It shows an excellent agreement between the LBM result and the analytical solution at all a values. The derivations of the computed shear stress from the LBM simulations are in the range of 10^{-7}–10^{-11} for different a values, again in excellent agreement with the zero value according to the analytical solution.

In addition to the velocity, pressure, the stress fields, K_x and K_y, we also compute the following normalized projection of the pressure field [29]

$$P_2(t) = -\frac{8}{\rho_0 U_0^2}\left\langle p(x,y,t)\cos\left[k_L(x+y)\right]\cos\left[k_L(x-y)\right]\right\rangle. \tag{62}$$

And $P_2(t)$ evolves as $e^{-2k^2\nu t}$ for the analytic solution.

In Fig. 13, we show $P_2(t)$ obtained from the LBM simulations, as a function of dimensionless time, for different a values. The curves contain low-level acoustic oscillations initially for some a values, similar in magnitude to what was observed in [29]. In the cases with smaller a, the oscillations are relatively weaker, as seen in Fig. 13(a). The acoustic oscillations gradually disappear at long times for all cases, leading to an excellent agreement of the simulated P_2 values with its analytical solution, as seen in Fig. 13(b).

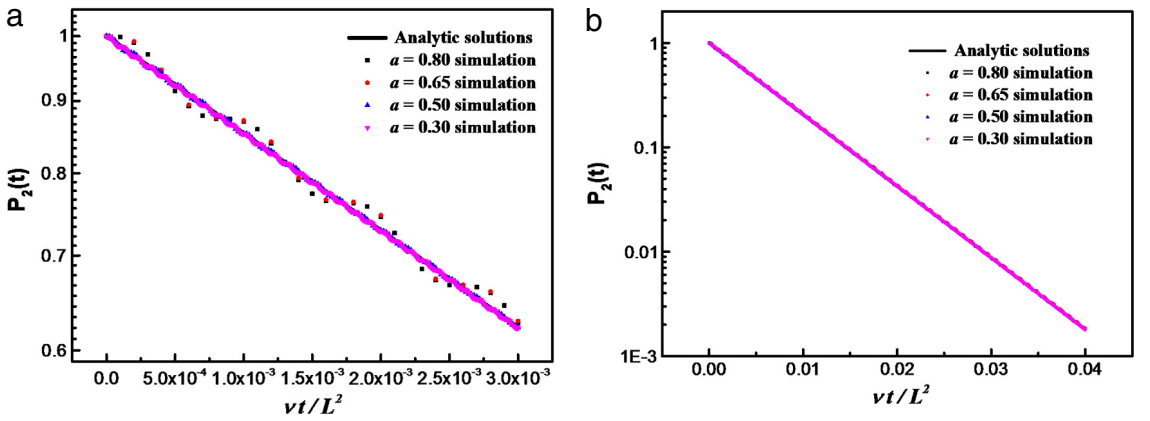

Fig. 13. $P_2(t)$ as a function of dimensionless time, obtained from the LBM simulations using different a values. The analytical solution is also shown. (a) Short time; (b) long time.

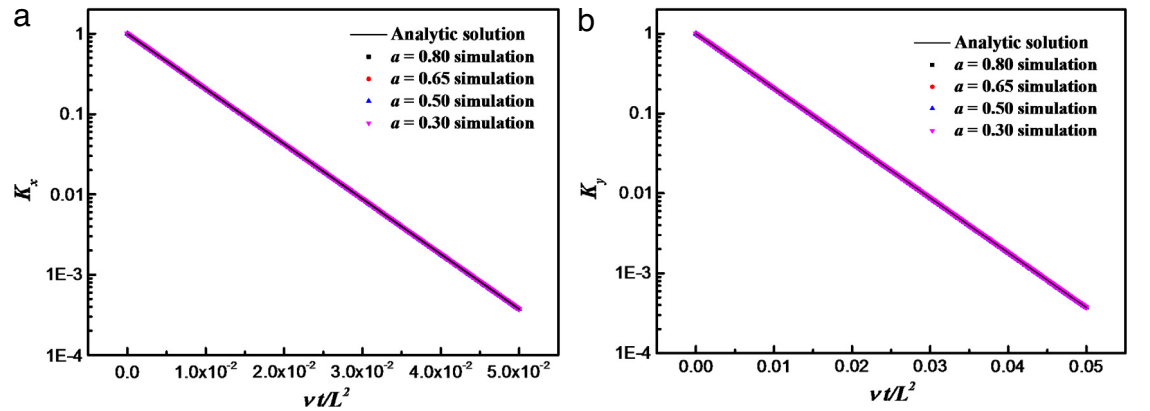

Fig. 14. The component kinetic energy as a function of time, obtained from our LBM simulations with different a values: (a) K_x; (b) K_y. The analytical solution is also shown.

On the other hand, the simulated K_x and K_y values are smooth at all times and are consistent with the analytic solution, as shown in Fig. 14. These demonstrate that the non-equilibrium moments have been properly initialized.

Motivated by the discussions in [28], we next demonstrate the isotropy property of our new model by plotting the time evolution of $\langle K_x\rangle / \langle K_y\rangle$ in Fig. 15 for the case of $a = 0.5$ and $Re = 100$. Furthermore, the results from Bouzidi's model are also included. The parameters for Bouzidi's model are: $a = 0.50$, $Re = 100$, $U_0 = 0.055$, and the relaxation times are $s_e = 1.5195$, $s_n = 0.4966$, and $s_c = 0.9091$. These parameters lead to $\nu = 0.1100$, $\nu_x = 0.1396$, and $\nu_y = 0.0804$ in Bouzidi's model. Clearly, Fig. 15 shows that $\langle K_x\rangle / \langle K_y\rangle$ from Bouzidi's model oscillates around 1.0, which is related to the anisotropy of the transport coefficients. Since the flow is incompressible, any deviation from isotropy in the velocity field leads to pressure redistribution, which restores isotropy. This interaction between the velocity field and pressure field caused oscillations in both velocity and pressure fields, and therefore oscillations in the $\langle K_x\rangle / \langle K_y\rangle$ ratio. The magnitude of the oscillations increases with increasing time as the kinetic energy decays. The period of oscillations is about 377 LBM time steps, which is roughly equal to $L/\sqrt{2}c_s = 375$, where $c_s = 0.377$. However, for our new θ model, $\langle K_x\rangle / \langle K_y\rangle$ is always close to one; the maximum relative deviation is around 2×10^{-4}. This demonstrates convincingly that the isotropy property is satisfied by our new θ model.

Fig. 16 shows the velocity and pressure profiles at $x/L = 0.5$ for the case of $a = 0.5$ at $Re = 100$. The simulated results agree well with the analytical solution at all four selected times. Again, it illustrates that the velocity components in the x and y directions decay at the same rate. The excellent agreement between the LBM and the analytical solution is further shown for the normal stress field in Fig. 17.

5. Summary and concluding remarks

In this paper, we have shown, for the first time, that the D2Q9 MRT LBM model can be used on a rectangular grid to produce viscous flows that are fully consistent with the Navier–Stokes equations. The basic idea is to introduce a new

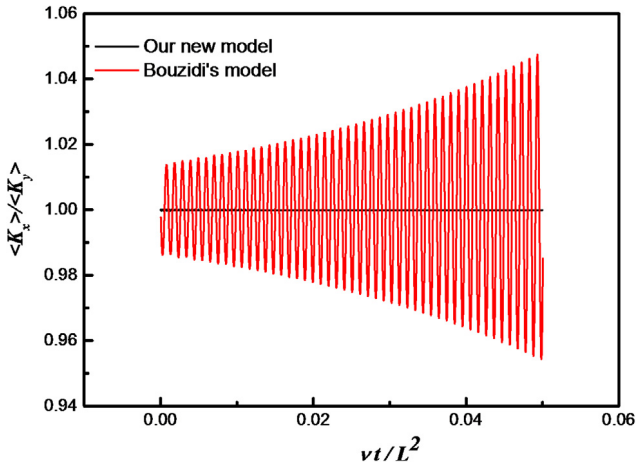

Fig. 15. The ratio $\langle K_x \rangle / \langle K_y \rangle$ plotted as a function of time from our new model for the case of $a = 0.5$ and $Re = 100$. The corresponding result for Bouzidi's model is also shown.

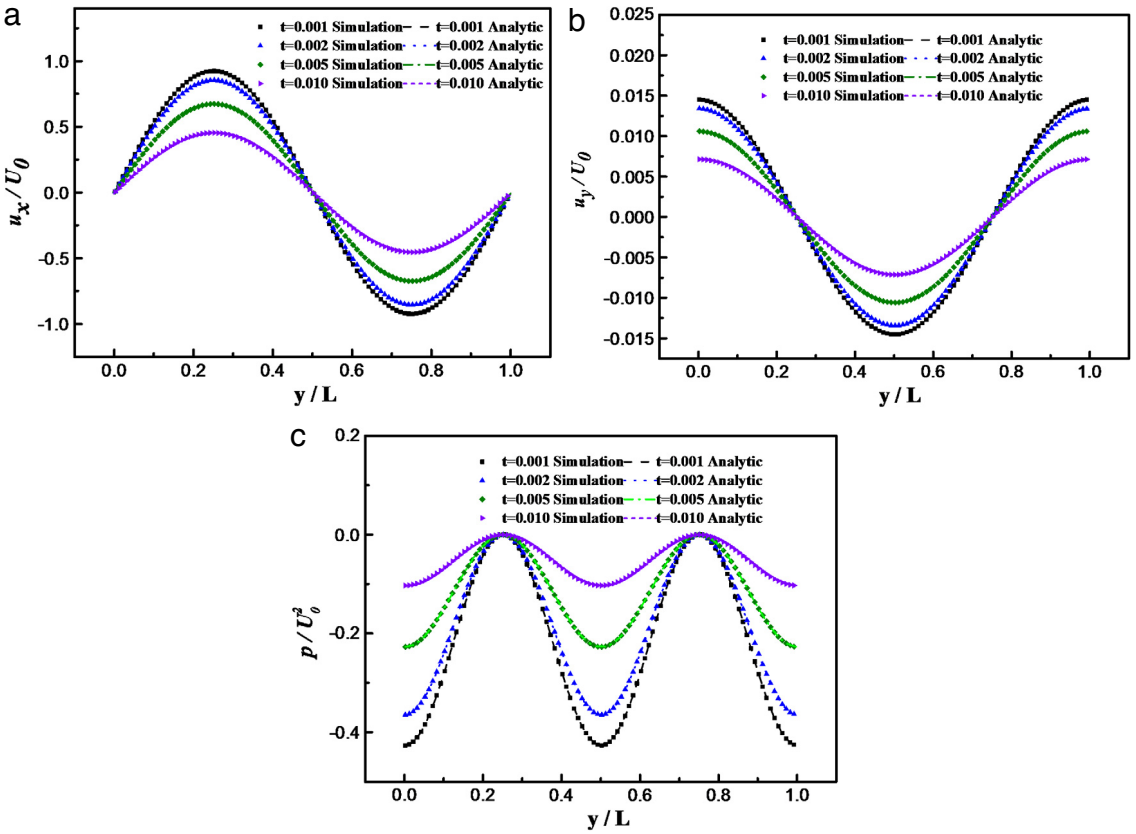

Fig. 16. The velocity and pressure profiles at $x/L = 0.5$ at several different dimensionless times (the time is normalized by $\nu t/L^2$): (a) u_x/U_0; (b) u_y/U_0; (c) $p/\rho_0 U_0^2$. The LBM results are shown by symbols and the analytical solutions are shown as lines. $a = 0.5$ and $Re = 100$.

adjustable parameter into the previous model of Bouzidi et al. [16]. This parameter amounts to a rotation in the 2D energy–normal stress moment subspace. We first re-derived the hydrodynamic equations of the two previous models [16,17] intended for a rectangular grid. By inverse design using the Chapman–Enskog multi-scaling analysis, we showed that these two previous models are unable to satisfy all isotropy conditions of the transport coefficients. At the Euler equation level, the two previous models are equivalent. Zhou's model could also be viewed as a rotation in the 2D energy–normal stress moment subspace relative to Bouzidi et al. [16]. But such rotation was fixed by Zhou's definition of the moments in order to use the a-independent transformation matrix. In our model, this rotation does not fix the transformation matrix,

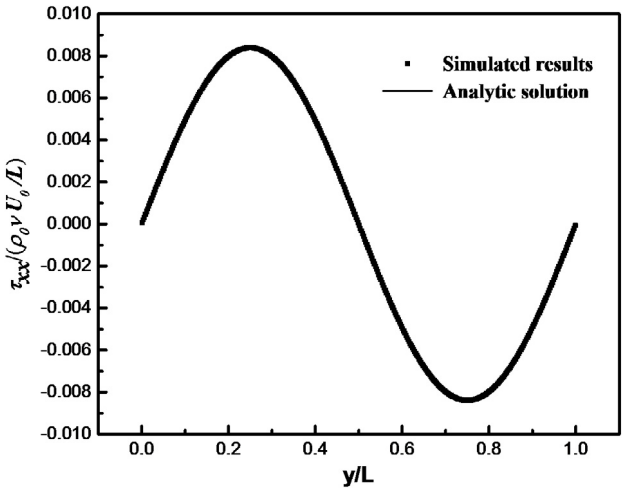

Fig. 17. Profile of normalized normal stress at $\nu t/L^2 = 0.04$ and $x/L = 0.5$. $a = 0.5$ and $Re = 100$.

which provides the necessary flexibility to restore the full isotropy of transport coefficients as required by the Navier–Stokes equation. Clearly, the success of our new model rests in part on the flexibility of relaxation parameters in the MRT LBM approach. Namely, the BGK LBM uses the same relaxation parameter for all moments, and is clearly unable to produce the necessary isotropy on a rectangular grid.

We showed, by the inverse design, that all equilibrium moments can be determined, except that for the energy squared moment which plays no role in the Navier–Stokes equation. Two conditions required to partially meet isotropy (the full isotropy has three conditions) are identified, and are shown to yield the two coupling relationships derived previously in Bouzidi et al. [16] using a very different approach. These partial conditions allow all departures from isotropy be expressed in terms of a single quantity. The additional parameter θ in our model is then used to eliminate this term. We believe our inverse design and the partial isotropy conditions provide new insights into previous models as well as to better explain how our new model works from the theoretical perspective.

Our new model contains two adjustable parameters, the speed of sound c_s, and a parameter γ defining the energy flux. Their values can be optimized for the use of smaller aspect ratio a, the best numerical stability, or for achieving a higher flow Reynolds number. In this paper, we have demonstrated that $a = 0.2$ may be used (see Section 4.1). However, we find that, in general, the model tends to be unstable when $a < 0.2$. The smallest value of a that can be achieved also depends on the nature of the flow and the flow Reynolds number, and the relaxation parameters for non-essential modes. A systematic study of the numerical stability for the parameter space formed by c_s, γ, and the relaxation parameters for non-essential modes, for a given a, is beyond the scope of this paper, and will be reported in a future paper.

We have also validated our new model using the 2D channel flow, 2D lid-driven cavity flow, and 2D decaying Taylor–Green vortex flow. We showed that the new model yields excellent results that are independent of the value of the grid aspect ratio a. For the channel flow, the second-order accuracy is confirmed with mid-way bounce back boundary conditions. For the cavity flow, we showed how to treat a moving wall within our new model. In the case of the Taylor–Green vortex flow, the results show that our new MRT model can ensure the isotropy of the transport coefficients on a rectangular lattice. Again our results are in excellent agreement with those reported in the literature. Numerical tests show that our model is numerically stable for small a and for high flow Reynolds numbers.

Finally, we note that there are alternative methods to restore isotropy. For example, by using two more microscopic velocities, Hegele et al. [18] were able to meet this goal in 2D. However, our model does not require any addition of microscopic velocities. We also believe that our idea can be applied in 3D to allow the use of non-cubic grids, instead of the cubic grid for standard models. This possibility will be reported in the near future.

Acknowledgments

This work has been supported by the US National Science Foundation (NSF) under grants CBET-1235974 and AGS-1139743 and by Air Force Office of Scientific Research under grant FA9550-13-1-0213. LPW also acknowledges support from the Ministry of Education of PR China and Huazhong University of Science and Technology through Chang Jiang Scholar Visiting Professorship (J2011028). YZ also acknowledges support from 973 project of Ministry of Science and Technology of China (No. 2012CB720500) and the National Natural Science Funds of China (NSF21406059). YZ also acknowledges support by the Fundamental Research Funds for the Central University (WA222201314020).

References

[1] S. Chen, G. Doolen, Lattice Boltzmann method for fluid flows, Annu. Rev. Fluid Mech. 30 (1998) 329–364.
[2] D. Yu, R. Mei, L.-S. Luo, W. Shyy, Viscous flow computations with the method of lattice Boltzmann equation, Prog. Aerosp. Sci. 39 (2003) 329–367.
[3] T. Inamuro, T. Ogata, S. Tajima, et al., A lattice Boltzmann method for incompressible two-phase flows with large density differences, J. Comput. Phys. 10 (2004) 628–644.
[4] M.E. McCracken, J. Abraham, Multiple-relaxation-time lattice Boltzmann model for multiphase flow, Phys. Rev. E 71 (2005) 036701.
[5] H.P. Fang, Lattice Boltzmann method for simulating the viscous flow in large distensible blood vessels, Phys. Rev. E 5 (2002) 051925.
[6] L.-P. Wang, B. Afsharpoya, Modeling fluid flow in fuel cells using the lattice Boltzmann approach, Math. Comput. Simul. 72 (2006) 242–248.
[7] H. Gao, C.Q. Qiu, D. Fan, Y. Jin, L.-P. Wang, Three-dimensional microscale flow simulation and colloid transport modeling in saturated soil porous media, Comput. Math. Appl. 59 (2010) 2271–2289.
[8] X.B. Nie, G.D. Doolen, S.Y. Chen, Lattice–Boltzmann simulations of fluid flows in MEMS, J. Stat. Phys. 107 (2002) 279–289.
[9] J.F. Zhang, Lattice Boltzmann method for microfluidics: models and applications, Microfluid. Nanofluid. 10 (2011) 1–28.
[10] O. Filippova, D. Hänel, Boundary-fitting and local grid refinement for lattice-BGK models, Internat. J. Modern Phys. C 9 (1998) 219–228.
[11] O. Filippova, D. Hänel, Grid refinement for lattice-BGK models, J. Comput. Phys. 147 (1998) 1271–1279.
[12] D. Yu, R. Mei, W. Shyy, A multi-block lattice Boltzmann method for viscous fluid flows, Internat. J. Numer. Methods Fluids 39 (2002) 99–120.
[13] X. He, L.-S. Luo, M. Dembo, Some progress in lattice Boltzmann method. 1. Nonuniform mesh grids, J. Comput. Phys. 129 (1996) 357–363.
[14] X.D. Niu, Y.T. Chew, C. Shu, Simulation of flows, around an impulsively started circular cylinder by Taylor series expansion- and least squares-based lattice Boltzmann method, J. Comput. Phys. 188 (2003) 176–193.
[15] J.M.V.A. Koelman, A simple lattice Boltzmann scheme for Navier–Stokes fluid flow, Europhys. Lett. 15 (1991) 603–607.
[16] M. Bouzidi, D. d'Humières, P. Lallemand, L.S. Luo, Lattice Boltzmann equation on a two-dimensional rectangular grid, J. Comput. Phys. 172 (2001) 704–717.
[17] J.G. Zhou, MRT rectangular lattice Boltzmann method, Internat. J. Modern Phys. C 23 (2012) 1250040-1–1250040-17.
[18] L.A. Hegele Jr., K. Mattila, P.C. Philippi, Rectangular lattice-Boltzmann schemes with BGK-collision operator, Phys. Rev. E 83 (2011) 048701.
[19] P. Lallemand, L.S. Luo, Theory of the lattice Boltzmann method: Dispersion, dissipation, isotropy, Galilean invariance, and stability, Phys. Rev. E 61 (2000) 6546.
[20] D. d'Humières, I. Ginzburg, M. Krafczyk, et al., Multiple-relaxation-time lattice Boltzmann models in three-dimensions, Philos. Trans. R. Soc. Lond. Ser. A Math. Phys. Eng. Sci. 360 (2002) 437–451.
[21] Z. Guo, C. Zheng, B. Shi, Discrete lattice effects on the forcing term in the lattice Boltzmann method, Phys. Rev. E 65 (2002) 046308.
[22] Q. Zou, X.Y. He, On pressure and velocity boundary conditions for the lattice Boltzmann BGK model, Phys. Fluids 9 (1997) 1591–1598.
[23] I. Ginzbourg, P.M. Adler, Boundary flow condition analysis for the three-dimensional lattice Boltzmann model, J. Phys. II France 4 (1994) 191–214.
[24] M. Cheng, K.C. Hung, Vortex structure of steady flow in a rectangular cavity, Comput. & Fluids 35 (2006) 1046–1062.
[25] A.A. Mohamad, A. EI-Ganaoui, R. Bennacer, Lattice Botlzmann simulation of natural convection in an open ended cavity, Int. J. Therm. Sci. 48 (2009) 1870–1875.
[26] Y. Peng, C. Shu, Y.T. Chew, A 3D incompressible thermal lattice Boltzmann model and its application to simulation natural convection in a cubic cavity, J. Comput. Phys. 193 (2004) 260–274.
[27] U. Ghia, K.M. Ghia, C.T. Shin, High-Re solution for incompressible flow using Navier–Stokes equations and a multigrid method, J. Comput. Phys. 48 (1982) 387–411.
[28] S. Chikatamarla, I. Karlin, Comment on "Rectangular lattice Boltzmann method", Phys. Rev. E 83 (2011) 048701.
[29] R.W. Mei, L.S. Luo, P. Lallemand, D. d'Humieres, Consistent initial conditions for lattice Boltzmann simulations, Comput. & Fluids 35 (2006) 855–862.